MICRO-SCALE PARAMETRIC ANALYSIS OF INDEPENDENT COMPONENTS OF A MASONRY WALL SYSTEM

A Thesis

by

MIGUEL FERNANDO ORTIZ CAHUN

Submitted to the Office of Graduate and Professional Studies of
Texas A&M University
in partial fulfillment of the requirements for the degree of

MASTER OF SCIENCE

Chair of Committee,	Zenon Medina-Cetina
Committee Members,	Arash Noshadravan
	Homero Castaneda-Lopez
Head of Department,	Robin Autenrieth

May 2018

Major Subject: Civil Engineering

ABSTRACT

This study presents preliminary results of the modeling of all different testing components of a masonry wall when these components are subjected to unconfined compression: mortar cube, mortar cylinder, and concrete block compression (meso-scale structures), by the use of 2D and 3D Discrete Element Method (DEM). The purpose of this investigation is to calibrate the mortar cylinder and the concrete block using their corresponding numerical DEM model and to perform a parametric analysis for each of their sets of micro-parameters. The micro-parameters' influence on the model behavior is analyzed, and a broad comparison between the materials micro-properties is presented. The specimens were calibrated with experimental data obtained from previous experimental tests realized at Universidad Autonóma de Yucatán (México). The initial calibration was completed based on meso-parameters populated from the experimental data. Besides the materials' micro-parameters, other control variables are analyzed such as shape (cube and cylinder) and the modeling dimension approach (2D and 3D) for the case of the mortar. Models showed to be more brittle than the experimental data. A parametric analysis was carried out to understand the independent influence of each micro-parameter on the macro-behavior of each specimen. PFC 2D/3D by Itasca was the software used to perform the simulations of all compression tests. Results showed difficulties when predicting the stress – strain curve, being able to predict the peak stresses. Also, comparison between geometry and dimension approach showed inconsistency when comparing 2D and 3D in the mortar case. Results will be used in a future study for the probabilistic multi-scale calibration of the masonry wall systems, from the independent wall components to the full macro-scale system response submitted to lateral cyclic loads.

DEDICATION

This work is dedicated to my parents who have been the foundation of my life and always has encouraged me to pursue my dreams.

ACKNOWLEDGEMENTS

First, I would like to thank my advisor, Dr. Zenon Medina-Cetina, who has always guided me throughout my studies abroad. His constant encouragement to improve my work and education has left a significant impact on this work and my life.

To all my committee members, Dr. Homero Castaneda-Lopez, and Dr. Arash Noshadravan, who have been supportive and suggestive about this research work. A special mention to Dr. Luis Enrique Fernandez Baquiero who approved the usage of the experimental data and moreover, he has guided me since my Bachelor studies.

I am deeply grateful to the staff at Texas A & M University, from which I always received a kind and humane treatment during my master's studies.

Finally, I would like to thank my family, from which I only have been receiving support and kindness my entire life. Without their love and companionship, I would not have been able to complete this goal.

CONTRIBUTORS AND FUNDING SOURCES

This work was supervised by a thesis committee consisting of Dr. Zenon Medina-Cetina, Dr. Arash Noshadravan the Department of Civil engineering and Dr. Homero Castaneda-Lopez of Material Science and Engineering Department. All work for the thesis was completed independently by the student.

Graduate study was supported by Consejo Nacional de Ciencia y Tecnología (CONACYT) who provided funding to the student covering tuition and living expenses.

TABLE OF CONTENTS

Page

LIST OF FIGURES

Page

LIST OF TABLES

Page

CHAPTER I

INTRODUCTION

I.1 Problem statement

Composite materials are either used when the properties of a material must be improved or to reduce the production costs when considerable amount of material is required. Mortar and cement are two such composites that are widely used in the construction industry. Cement, sand, and lime are the main constituents of mortar; while cement, sand, and gravel are the main constituents of concrete. Blocks made of mortar and cement were chosen to be investigated because they are essential components of masonry walls.

Masonry systems have been built worldwide during centuries. Furthermore, the historic preservation of many of them is of significant matter[1]. Just in Mexico alone, masonry construction methods represent around 50% of all existing structures[2]. Determination of safety of masonry structures is paramount for a variety of initial and boundary conditions as well for a variety of material properties [3]. The extensive usage of masonry systems has driven to investigate the behavior of these walls and its components. Traditionally, the study was carried out by creating meso-scale models (mortar cube and cylinder) and macro-scale models (buildings and masonry walls), submitting them to experimental tests and then analyzing the behavior observed.

However, the advancements in computational resources now make it feasible to use newer methods such as numerical modeling to study these behaviors. These mathematical models can help predict the behavior of complex structures subjected to different loading scenarios and boundary conditions. However, the calibration of numerical model parameters is a fundamental process for the generation of accurate predictions.

Asteris and Plevris [1] categorized numerical modeling into two possible categories: macro-modeling and micro-modeling. Finite Element Method (FEM) is a macro-modeling method which permits the idealization of the masonry wall as a homogenized continuum model and, thus, contemplates the effect of mortar joints implicitly. On the other hand, micro-modeling examines the mortar–block interface explicitly. Micro-modeling methods can be categorized as follows: Discontinuous – Finite Element Method (D-FEM), Discrete/Distinct Element Method (DEM), Discontinuous Deformation Analysis (DDA) and Finite-Discrete Element Method (FDEM).

I.2 Literature review of numerical methods for studying masonry walls

I.2.1 Finite element method (FEM)

A widely used numerical method is the Finite Element Method, which is based on partial differential equations that cannot be solved by analytical arrangement. Instead, an approximation of the equations can be constructed upon discretization methods. These methods conduct a solution by analytical models equations, which can be work out by numerical systems[4].

FEM permits to create a model of masonry wall under different boundary conditions. It is also the most common approach due to its relatively low computational resources demand. However, as it represents a good approach, it has a difficulty when discontinuities are intended to be represented[3]. Hence, researchers have created strategies to include those discontinuities within its FEM models. Stavridis and Shing [5] developed different approaches using FEM to calibrate the seismic performance of reinforced concrete frames with masonry infill. Campbell Barraza [6] created a FEM model capable of representing different configurations of masonry walls (reinforced, unreinforced, confined masonry), size of the bricks and joints. Also, he considered a joint model defined as a special connection considering two nonlinear springs and a contact element. Lizárraga and Pérez Gavilán [7] modeled confined masonry walls with clay bricks,

submitted to axial loaded and cyclic lateral load. They used Laurenco [8] method for modeling masonry structures. Compounded interface with nonlinear properties can reproduce shear, tension and compression failure.

In the meso-scale, authors have used FEM for modeling the masonry components. Gonzalez Herrera [9] conducted a study in which he tested piles of hollow blocks. Then with his experimental data created a FEM model to know the stress distribution along the three-layer pile of concrete blocks. Similarly, it is possible to simulate concrete under tensile test (Brazilian test). Indriyantho and Nuroji [10] created a FEM model to further explain the internal stresses in the cylinder under the tensile test.

In recent years finite element analysis includes the creation of interface elements, which are capable of representing most of the failure mechanisms[6-8, 11]. This method also requires low computational resources when compared with discontinue approaches. It can be applied to large-scale models which provides an understanding of the global behavior structure[12].However, when the model intends to be sophisticated the number of parameters increase, consequently, it requires more computational resources. Also, creating new contacts or re-meshing when large deformation occur, is not easy to provide[1].

I.2.2 Finite – discrete element method (F-DEM)

In recent days, researchers have taken advantage of FEM and DEM and combined them. F-DEM was introduced by Munjiza [13] for solving fracturing problems. The main idea is to consider deformable bodies that can be split and separate during the analysis process. The interaction between discrete elements is considered through the contact algorithm for the normal forces and the Coulomb law for friction.

The combined F-DEM is used for modeling different masonry structures, and its conception is to model from the continuum to the discontinue[14]. Masonry buildings have been analyzed using F-DEM. Smoljanovic et al. [15] present an analysis of a dry-stone masonry structure under monotonic, cyclic seismic loads. They used F-DEM for modeling strategy. The stone blocks were model as a discrete element which is discretized by triangular finite element. Erdogan et al. [16] used this method for modeling the 57th infantry memorial in Turkey. They used Ansys/LSDYNA software to create the F-DEM model. The modeling procedure was similar to Smoljanovic et al. [15] used for modeling the stone block, and the mortar effect was neglected due to its low strength.

Smoljanovic et al. [17] presented a model capable of reproducing the behavior of dry-stone masonry building under in-plane and out-plane loading scenarios. Yuen and Kuang [18] tested reinforced masonry walls under simultaneously in-plane and out-plane loading scenarios. He used F-DEM to model his experimental observations. This research work is focused on creating a correlation between these two loading scenarios.

F-DEM has proven its functionality modeling masonry structures and the discontinuities it implies. This model approach allows large displacements and rotations with complete detachment of blocks. Nonetheless, this model is mostly used on macro-scale models and is not suitable for studying meso-scale models such as the mortar cylinder and cube or the concrete block as individuals[19].

I.2.3 Discrete element method

The Discrete Element Method was introduced by Cundall and Strack [20], and it is widely used in fracture mechanics and soil interaction modeling. It is used in the mining, manufacturing and civil engineering industries. DEM is a particle-based modeling method that allows complete

particle detachment and high deformation of the specimens. In geomechanics is used mostly for material modeling by applying different initial, boundary and loading conditions.

Çakti et al. [3] used DEM to model a scale representation of the Mustafa Pasha Mosque in Skopje subjecting it to a shake table test. They chose this method primarily because it made it possible to simulate the crack propagation along the brick interface and the discontinuities between blocks. Sarhosis et al. [21] modeled a masonry wall with openings using the commercial software UDEC [22] and studied its behavior under axial load actions. Their DEM model could represent different stages; from initial crack development to crack propagation at stages of increased loading and ultimately the mode of failure. Isfeld and Shrive [23] modeled walls from The Prince of Wales Fort in Manitoba, Canada and then submitted it to harsh weather conditions, due to which it showed deterioration and deformation. Calibration was trial and error, and it was their primary task.

Given the complexity of masonry structures, assigning the appropriate material properties is a difficult task. Çakti et al. [3]considered a rigid block behavior, as a consequence, all the system deformation was lumped at the joints. Standard calibration is carried out by trial and error, as previous works have presented [3, 21, 23].

In order to better understand the behavior of the mortar-brick interface, it is first necessary to understand the behavior of each element individually under different loading scenarios. A classic test for mortar is the compression cube test in which a 5 X 5 cm mortar cube is subjected to a uniaxial compression load. Modeling the same using DEM is possible. Watters [24]created a DEM of a mortar cube loaded uniaxially that reproduced his experimental tests. Gyurko and Borosnyoi [25] created a DEM model using PFC3D (Particle Flow Code) software of a concrete cube submitted to uniaxial load. The major objective of this work is to simulate the material behavior to assess better micro parameters based on meso-scale experimental observations. Riera et al. [26]

created a DEM of a concrete cylinder submitted to the tensile test (Brazilian test). Their main purpose was to study the influence of the width of the strip used for performing this test. Gyurko and Borosnyoi [25] presented a DEM representing a concrete cube under the indentation test. They used parallel bonding as a contact model between the particles and used PFC3D for modeling their specimens.

The use of DEM is particularly suitable to simulate shearing failure mechanisms in masonry structures[12, 27]. In this investigation, a meso-model, using the Discrete Element Method is used to simulate and study the behavior of a mortar cylinder, a mortar cube, and a concrete block called from herein *specimens*. The usage of micro modeling enables the identification of the control parameters that help predict stress-strain material behavior. Moreover, a discrete element model will be implemented since it allows the use of contact models between particles inside the specimens. This model will later be calibrated to match the behavior of the specimens observed experimentally by Hernandez Santillan [28] and Ortiz Cahun [29] at a meso-scale level.

I.3 Objectives

- To model a mortar cylinder (15 cm diameter x 30 cm height), a mortar cube (5 cm x 5 cm) and a hollow concrete block (15 cm x 20 cm x 40cm) specimens by the use of the Discrete Element Method.
- To calibrate the proposed specimens' models using laboratory experimental observations.
- To analyze the influence of each specimens' model microscopic parameters on their mechanistic response at the mesoscale.

I.4 Hypothesis

Standard masonry system components under compression can be modeled using 2D and 3D particle mechanics and reproduce the stress-strain behavior of laboratory tests.

I.5 Thesis Outline

Chapter II introduces the Discrete element method theoretical framework of the Particle Flow Code model in PDF3D and PFC2D.

Chapter III introduces the experimental design and the methodology used for creating the specimens' models in PFC2D and PFC3D.Also, the parametric analysis is explained and the procedure to analyze the micro-parameters' influence on the specimen model.

Chapter IV presents the results of the simulations and the parametric analysis. Each experiment will have section. Therefore, this chapter is organized by subsections corresponding to each experiment established in Chapter III. Also, discussion of results is presented after every subsection.

Chapter V provides the conclusions of this research work and pronounces future work.

CHAPTER II

DISCRETE ELEMENT METHOD (DEM)

The discrete element method can be described as particle-based modeling which uses either disk or spheres to discretize an element. It uses Newton's laws and the kinematics calculation to compute forces and update the particle position in the simulation. This method was first introduced by Cundall and Strack [20], and it is widely used in fracture mechanics and soil interaction modeling. This method allows finite displacements and rotations of discrete bodies (including complete detachment) and recognizes new contacts automatically as the calculation progresses. The contact forces of an assembly of particles are calculated by tracking the movement of individual particles. DEM displacement-force calculation cycle is explained in Figure 1.

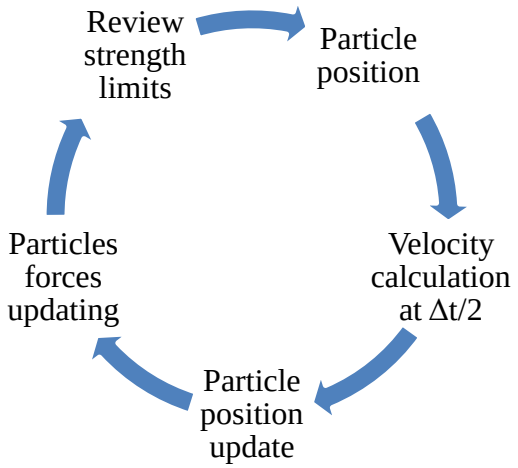

Figure 1. Force-displacement law kinematic process interaction [30].

II.1 Contact between particles

There are two types of contacts, the ball-ball contact and the ball-facet (wall). The ball- ball contact can be described as shown in **Figure** 2 and assumes that the total contact force can be decomposed into shear and normal components. The normal component acts along the direction of the normal vector to calculate the relative normal displacement via the force-displacement law. The shear component operates on the contact plane (perpendicular to the normal vector) to compute the incremental force and displacement. The contact gap is the minimal distance between the particles surfaces and is negative when the two particles are overlapped. The normal force is calculated at every update using the following relation [30]:

$$F_i^n = k^n \Delta U_i^n \qquad (2.1)$$

Where:

$F_i^n$is the linear normal force.

k^n is the normal stiffness of the contact.

ΔU_i^n is the particle surface overlap.

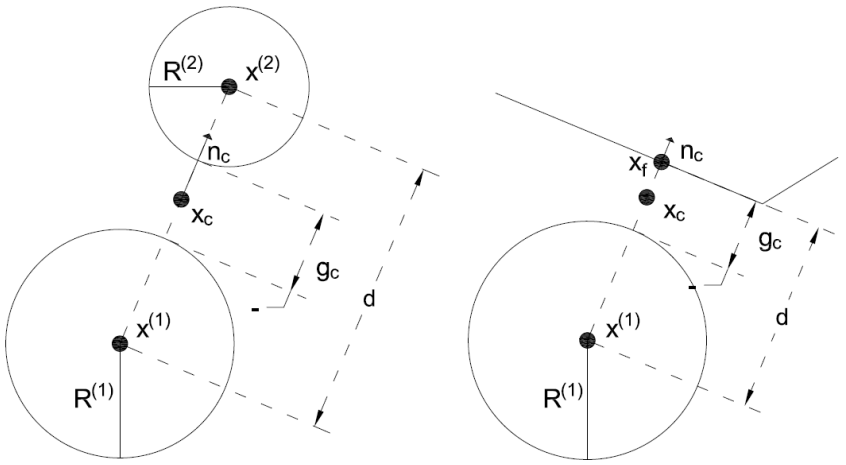

a) b)

Figure 2. Contact type. a) Particle-particle, and b) Wall-particle. [22]

The shear force follows an incremental time step calculation. The total force is zero once the particles assembly is created and reaches equilibrium with to respect each other. Incremental shear-displacement (ΔU_i^s) adds elastic shear force.

$$F_i^s = F_{i-1}^s + k^s \Delta U_i^s \tag{2.2}$$

II.2 DEM kinematic process

The PFC uses a numerical solution for the dynamic behavior. The time stepping algorithm assumes the velocities and accelerations as constant during the process. Also, the time step considered should be small such that, during a single time step, disturbances cannot propagate from any particle farther than its immediate neighbors.

The motion of a single rigid particle is determined by the resultant force and moment vectors acting upon it and can be described in terms of the translational motion of a point in the particle

and the rotational motion of the particle. The movement of the center of mass is described with regards to its position, velocity, and acceleration. The rotational motion of the particle is defined in terms of its angular velocity and angular acceleration[22]. In **Equation 2,** *F* is the resultant force, *m* is the particle's mass, and *g* is the body force acceleration vector.

$$F = m(\ddot{x} - g) \tag{2.3}$$

Now suppose that at any time *t,* **Equation 2.4** is solved. Now we want to calculate the new particle position by first calculating the particle velocity ($\dot{x}$) at a ½ time step of Δt. Then apply the result into the position updating formula as shown in the equation.

$$\dot{x}^{(t+\frac{\Delta t}{2})} = \dot{x}^{(t)} + \left(\frac{1}{2}\right)\left(\frac{F^t}{m} + g\right)\Delta t \tag{2.4}$$

$$x^{(t+\frac{\Delta t}{2})} = x^{(t)} + (\dot{x}^{(t+\frac{\Delta t}{2})})\Delta t \tag{2.5}$$

During the force-displacement cycling point, the forces are revised leading to velocity and acceleration update.

$$\dot{x}^{(t+\frac{\Delta t}{2})} = \dot{x}^{(t)} + \left(\frac{1}{2}\right)\left(\frac{F^{t+\Delta t}}{m} + g\right)\Delta t \tag{2.6}$$

For the rotational motion, the same procedure is followed. Therefore, the rotational motion is evaluated by **Equation 2.7**.

$$M = \left(\frac{2}{5}\right)(mR^2)\dot{\omega} \tag{2.7}$$

Similar to the translational motion calculations, we want to now calculate the new particle rotation by first calculating the particle angular velocity ($\dot{\omega}$) at a ½ time step of Δt.

$$\omega^{(t+\frac{\Delta t}{2})} = \omega^{(t)} + \frac{1}{2}(\frac{M^{(t)}}{I})\Delta t \quad (2.8)$$

During the force-displacement cycling point, the forces and moments are revised, leading to velocity and acceleration update as shown in **Equation 2.9**.

$$\omega^{(t+\Delta t)} = \omega^{\left(t+\frac{\Delta t}{2}\right)} + \frac{1}{2}(\frac{M^{(t+\Delta t)}}{I})\Delta t \quad (2.9)$$

II.3 Bonded-particle model (BPM) PFC Description

PFC 2D/3D has a variety of built-in contact models. Bonded-particle model (BPM) simulates the mechanical behavior of circular or spherical particles with a non-uniform sized distribution that might be bonded together at their contact points [31]. In fracture mechanics and soil modeling this method is widely used, and it gives the possibility of modeling particles and cement as a parallel bond.

BPM provides the behavior of two interfaces: one is an infinitesimal linear elastic (no-tension), a frictional interface that carries a force and the other is a finite-size, linear elastic, bonded interface that takes a force and a moment. The first interface is equivalent to the linear model meaning it does not resist relative rotation, and by imposing a Coulomb limit, on the shear force. When the second interface is bonded, it resists relative rotation, and its behavior is linear elastic until the strength limit is exceeded and the bond breaks, making it unbonded. Once un-bonded, it carries no load. The unbonded linear parallel bond model is equivalent to the linear model[22]. In **Figure 3** the rheological model and the Coulomb failure mechanism for this constitutive model are presented.

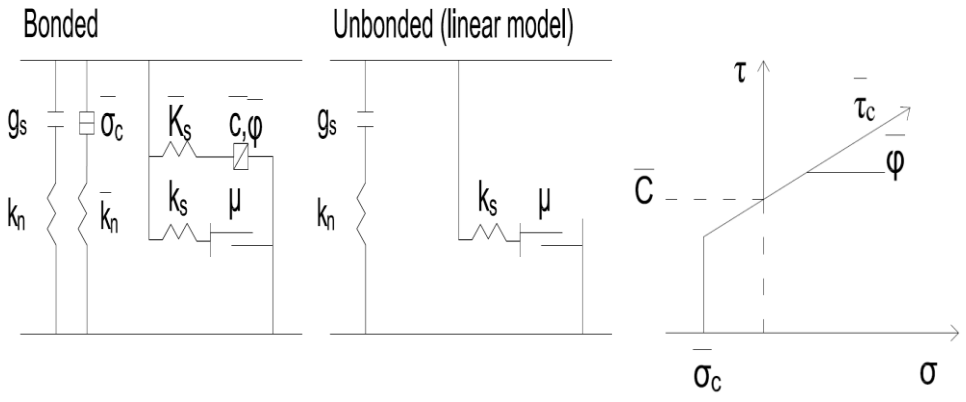

a) b)

Figure 3. Rheological model Bonded Particle Contact model, and Coulomb failure envelop[22].

The properties defined for the linear parallel bond are listed in Table 1. This table also includes the units used during simulations and the symbols used for further references. PFC and DEM, in general, can use more properties to describe this contact model. Nonetheless, in this investigation, these parameters are the only ones which are studied. In PFC documentation, it is possible to find alternative parameters for this contact model. In addition, it also includes a vast explanation on how to implement them in the simulation [22]. Potyondy and Cundall [31] and Zhang [30] report in their investigation the use of the parameters presented in this paper to create their respective specimens. Further explanation about the creation of the specimens is explained in this document.

Table 1. Material properties used in Bonded Particle Contact.

Symbol	Units	Material Properties
gs	m	Gap length
σ_c	Pascal	Tension strength
c	Pascal	Cohesion
Φ	Degrees^o	Friction angle
μ	No unit	Particle friction
E(LB)	Pascal	Young's Modulus
E(PB)	Pascal	Young's Modulus
k (LB)	No unit	Krat (kn/ks)
k(PB)	No unit	Krat (kn/ks)
Particle size	mm	
LB = Linear bond PB = Parallel bond		

Figure 4 explains the constitutive contact models for the different parameters included within the parallel bond model. In **Figure 4** (a) the tensile strength will work with an elastic deformation as long as the tensile strength is not exceeded, once it is exceeded the bond breaks and the linear model is used. The **Figure 4** (b) shows the twisting moment, relative twisting rotation and the shear stiffness for the bonded contact model interaction. Equally, as the tensile strength, the twisting moment will have an elastic deformation as long as its maximum value during the cycling is not exceeded. **Figure 4** (c) shows the shear strength constitutive model during bonded contact. During cycling, the deformation is linear elastic till the shear strength limit is not surpassed. The bending moment is as shown in **Figure 4** (d) and follows the same logic as the previous constitutive models.

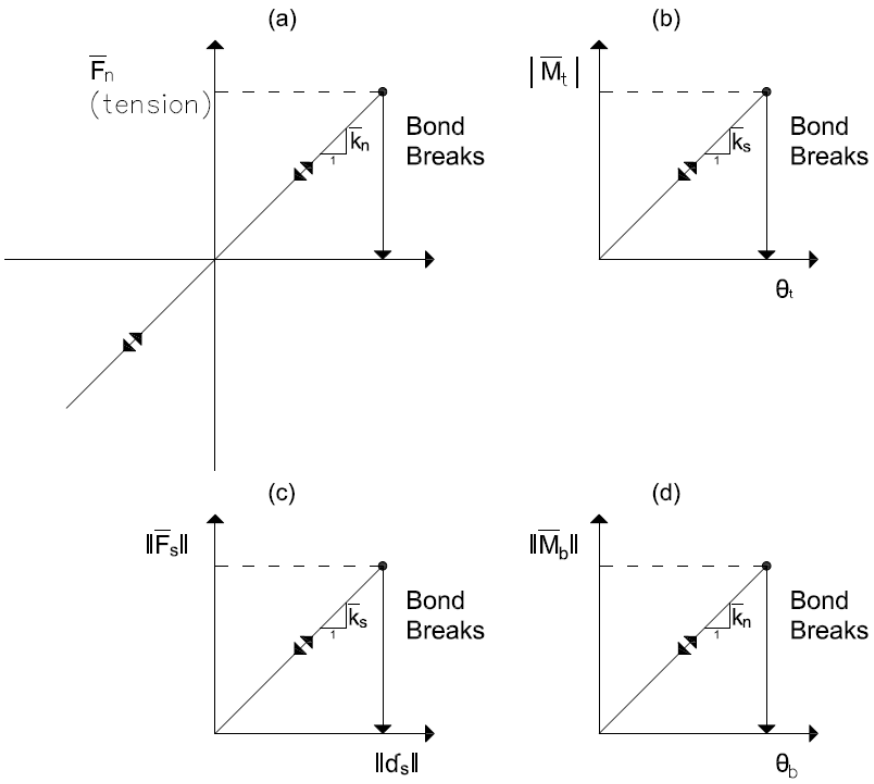

Figure 4. Normal force vs. parallel bond surface gap. (b) Twisting moment vs. relative twisting rotation. (c) Shear force vs. relative shear displacement. (d) Bending moment vs. relative bend rotation[22].

The force-displacement law for the parallel bond can be described in the following steps:

- Updating the bond cross-sectional properties:

$$\bar{R} = \bar{\lambda}\begin{cases} min(R^{(1)}, R^{(2)}), & ball - ball \\ R^{(1)}, & ball - wall \end{cases} \tag{2.10}$$

$$\bar{A} = \begin{cases} 2\bar{R}t, & 2D, t = 1 \\ \pi\bar{R}^2, & 3D \end{cases} \tag{2.5}$$

$$\bar{I} = \begin{cases} \frac{2}{3} t\bar{R}^3, & 2D(t=1) \\ \frac{1}{4}\pi\bar{R}^4, & 3D \end{cases} \tag{2.6}$$

$$\bar{J} = \begin{cases} 0, & 2D \\ \frac{1}{2}\pi\bar{R}^4, & 3D \end{cases} \tag{2.7}$$

Where $\bar{A}$ is the cross-sectional area, $\bar{I}$ is the moment of inertia of the parallel bond cross-section and $\bar{J}$ is the polar moment of inertia of the cross-sectional area.

- Updating the normal force on the contact:

$$\bar{F}_n = \bar{F}_n + \bar{k}_n \bar{A} \Delta\delta_n \tag{2.8}$$

Where $\Delta\delta_n$ is the relative displacement-increment.

- Updating the twisting moment:

$$\bar{M}_t = \begin{cases} 0\,, & 2D \\ \bar{M}_t - \bar{k}_s \bar{J} \Delta\theta_t, & 3D \end{cases} \tag{2.9}$$

- Updating of the bending moment:

$$\bar{M}_b = \bar{M}_b - \bar{k}_n \bar{I} \Delta\theta_b \tag{2.10}$$

- Updating the maximum normal and shear stresses:

$$\bar{\sigma} = \frac{\bar{F}_n}{\bar{A}} - \frac{\bar{\beta}\|M_b\|\bar{R}}{\bar{I}} \tag{2.11}$$

$$\bar{\tau} = \frac{\|\bar{F}_s\|}{\bar{A}} + \begin{cases} 0, & 2D \\ \bar{\beta}\frac{|\bar{M}_t|\bar{R}}{\bar{J}}, & 3D \end{cases} \tag{2.12}$$

Where β is the moment contribution factor [0,1].

- The last step is to review the strength limits. First, the tensile strength is checked. If the maximum allowed value is surpassed then the bond is broken, else, the shear strength is reviewed.

The updating of the formulation is explained above for the 2D and 3D version. In the 2D version, the twisting moment is not allowed. Therefore, calculations are shorter. Nonetheless, updating works the same for both cases, and the same numerical integration scheme is used.

CHAPTER III

EXPERIMENTAL DESIGN

According to the availability of experimental data, experiments are designed on each specimen. The concrete block and the mortar cylinder are the specimens to calibrate because in both cases exist the stress-strain curves of the unconfined compression test. For the case of the mortar cube, the peak stress is available. Therefore, two experiments are set for the mortar, and one experiment is set for the concrete block. Figure 5 is a diagram that summarizes the experiments performed on the mortar specimens.

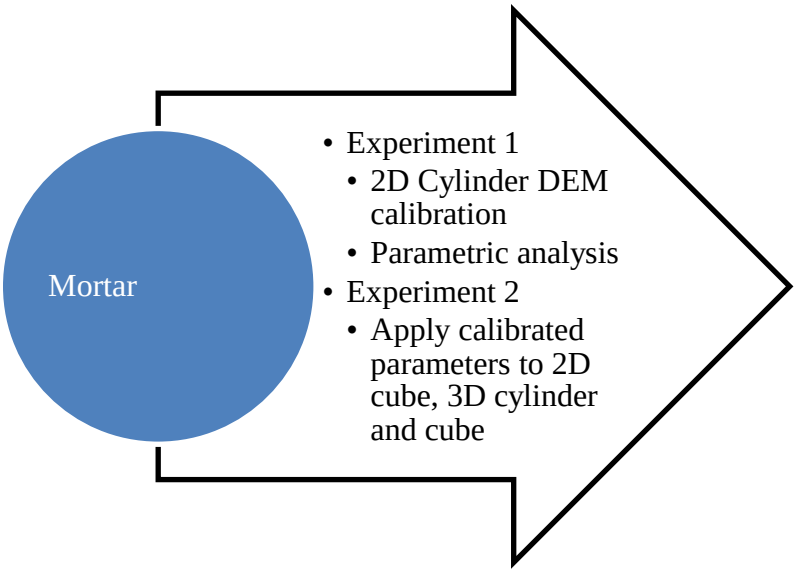

Figure 5. Diagram of experiments performed on mortar specimens.

Experiment 1 consists on create a 2D cylinder using PFC2D and then calibrate the model by fitting the stress-strain curve of the model with respect to the experimental data stress-strain curve. This initial calibration is used for the second stage that is to perform a parametric analysis which is explained in detail at following sections.

Experiment 2 consist on creating a 2D and 3D DEM of the mortar cube, and a 3D DEM of the mortar cylinder. Then, apply the parameters' values calibrated for the 2D mortar cylinder DEM.

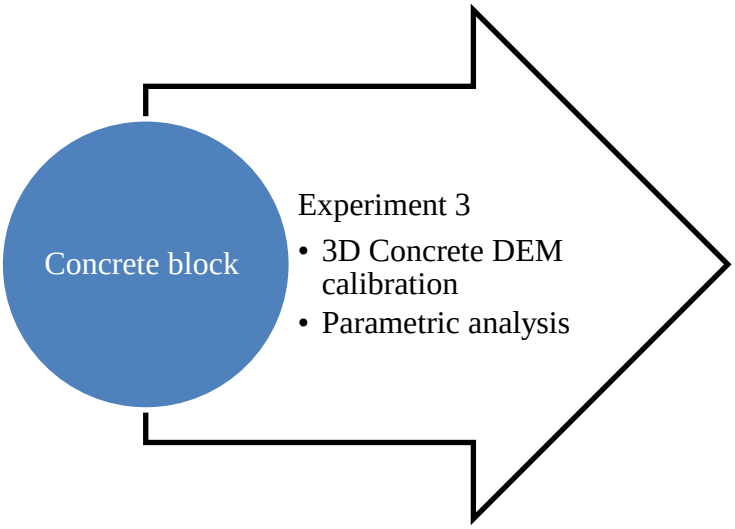

Figure 6. Diagram of the experiment performed on the concrete block

Experiment 3 consists of creating a 3D DEM of the concrete block and calibrate the model by fitting the stress-strain curve of the model with respect to the stress-strain curve of the experimental data. The second step in this experiment is to perform a parametric analysis similar to the experiment 1.

III.1 Specimen description

Hernandez Santillan [28] performed unconfined compression tests on mortar cylinders and hollow concrete blocks. Ortiz Cahun [29] also performed unconfined compression tests on mortar cubes to obtain the peak stresses. The material properties obtained from these two investigations are used in the simulations.

Table 2. BPM Experimental Material properties

Properties	Mortar Cube	Mortar Cylinder	Concrete block
Peak stress	3.39 MPa	2.75 MPa	5.33 MPa
Friction angle		10°	10°
Tension strength			0.29 MPa
Poisson ratio		0.2	0.2
D_{50} particle size	1.68E-3 - 2.00 E-3 m	1.68E-3 - 2.00 E-3 m	4.00E-3 -6.00E-3 m
Young Modulus (MPa)		7994 MPa	5246 MPa

The mortar used has the following proportion: 1: 2: 7 (cement, lime, and sand respectively). The median size of the particle used is 1.68 mm- 2.00 mm in a uniform distribution. For mortar, two different shapes are tested, cylinder and cube. In **Figure 7**, the mortar cylinder and cube characteristics are represented. The cylinder, shown in Figure 7(a), has 15 cm diameter and 30 cm height and the cube, shown in Figure 7 (b), is 5 (Depth) x 5 (width) x 5 (height) cm.

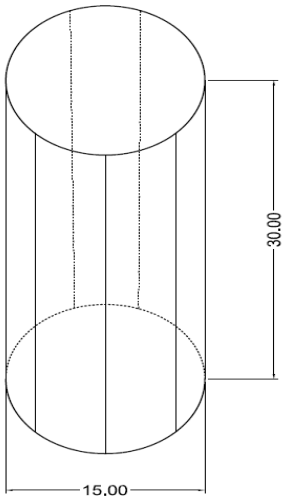

a) Mortar cylinder.

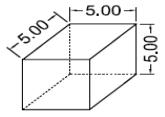

b) Mortar Cube.

Figure 7. Mortar specimens' dimensions(cm).

The concrete block has a depth of 15cm, a width of 20cm and a height of 40cm with particles ranging from a size of 4mm to 6mm, refer to **Figure 8**. The particle size is uniform because of the aggregates preparation mode. The gravel is washed leaving a minimum amount of fines. Therefore, and for the case of this study, the particle size is considered from 4.00-6.00 mm in a uniform distribution. This particle size corresponds to the size range of the aggregates used for the concrete block.

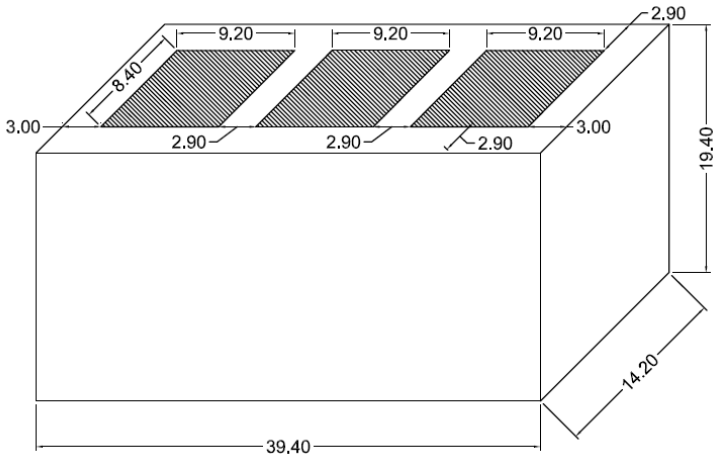

Figure 8. Concrete block dimensions(cm)

III.2 Material genesis

Material genesis follows similar procedures as experimental tests and is combined with modeling techniques. For both material assemblies, the same genesis logic is followed. The unique difference is in the modeling approach (2D/3D) and the geometry of the model. The material generation is similar to the work of Potyondy and Cundall [31]. They created a sandstone model using PFC3D and submit it to unconfined compression test and tensile compression test.

The initial step is to create a material vessel which will contain the particles without any constitutive model applied to them. The wall (or also called facet) stiffness should be higher than

the particle stiffness in order to ensure the particle do not trespass the wall and ensure the particle-wall overlap is as small as possible. **Figure 9** shows the creation of the 2D mortar cylinder. Blue lines represent the material vessel which contains particles at the beginning of the process. The red dots represent the particles.

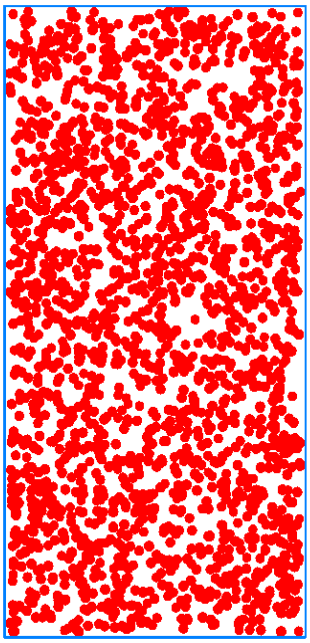

Figure 9. Material vessel and particle creation.

The sizes of the particles generated follow a uniform distribution from D_{min} to D_{max}. The particles are randomly generated having half the original size such that they do not overlap with each other. After the particle generation, the radii is increased to its final size, and the particles are permitted to rearrange under zero friction. During this process, the particle density is selected, and a linear model is used to describe the particle contact. The simulation will stop once the static equilibrium is reached. This process of relaxation will avoid locked-in stresses to develop within particle contacts, and also helps to evade particle overlapping. Once the equilibrium is reached,

the next step is dismantling the material vessel, deleting the lateral walls, while keeping the top and bottom walls intact for further use in the experimental simulation.

After this, the installation of parallel bonds is done. Particles contact with *gap* = (D_{min} /10) distance between their surfaces is considered close enough to apply the parallel bond. Parameters from **Table 1** are used at this stage. Note that locked-in forces can generate significant influence on specimen's response during simulations. In **Figure 10** the parallel bond concept is presented. Two plates or surfaces having the same size as of the particle diameter are idealized, such that more surface contact can be created between particles' contact.

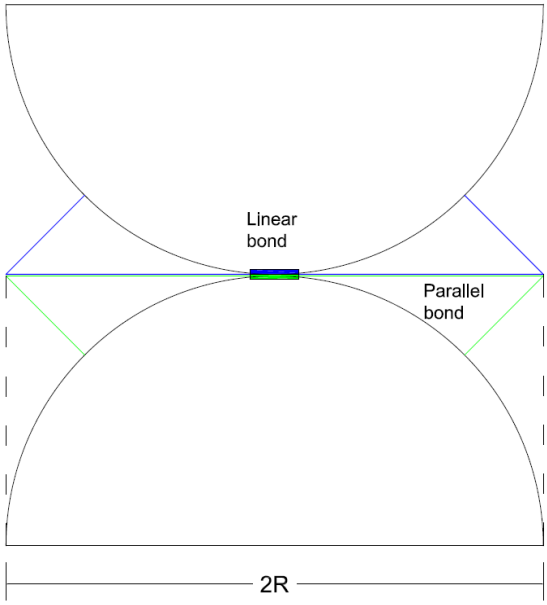

Figure 10. Parallel bond model [22].

The unconfined compression test now employs the use of the two remaining walls. The bottom wall is fixed, and by imposing a higher stiffness than particles on it, it does not allow the particles to trespass. The top wall is set with a strain rate of 0.10 s^{-1}. Refer to **Figure 11**.

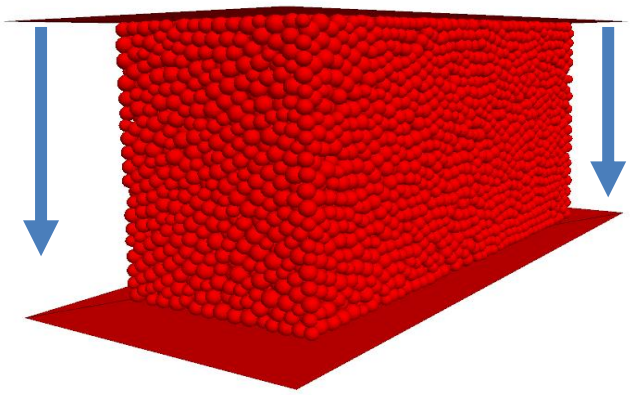

Figure 11. Unconfined compression test on the concrete block.

III.3 Choosing microparameters for DEM

Selecting a constitutive model for DEM is different as compared to the continuum models. The calibration of continuum model parameters is usually based on laboratory observations. However, in DEM the micro-parameter interaction is essential, and it must satisfy the macro-behavior of the specimen under the same experimental conditions. The micro-parameters needed for DEM calibration are usually unknown, and the calibration of a DEM model is done such that it represents the relevant material properties measured in experimental tests [31].

Calibration of the parameters is a trial and error process. This process starts with the application of experimental results such as tensile strength, Young's modulus, Poisson ratio, particle size and friction angle. Those parameters not found in the literature were assumed, such as cohesion strength, inter-particle friction, k (k_n/k_s). DEM's constitutive model named BPM (refer to section II.3) has two types of micro parameters; one for the linear bond, and the other for the parallel bond. Both cases share same parameters, such as Young's modulus and k. However, these two can possess different values and can be considered as separate variables. Nonetheless, the initial values

of these two micro-parameters is assumed to be equal, and later in the parametric analysis, their influence is analyzed.

Therefore, the experimental measurements are used in the initial calibration. Manual calibration, consisting of trial and error, is carried out to find a stress-strain curve that resembles the experimental behavior. These calibrated properties are then used as initial values for a parametric analysis that helps to predict the influence of each parameter on the overall behavior of the specimen.

Table 3. Initial parameters' values for the mortar cylinder and the concrete block

Symbol	Units	Material Properties	Mortar Initial	Concrete block Initial
Gap	m	Gap length	2.00E-04	2.00E-04
σ_c	Pascal	Tensile strength	3.00E+05	3.00E+05
c	Pascal	Cohesion strenght	3.00E+05	3.00E+05
Φ	Degrees^o	Friction angle	70.00	70.00
μ		Particle friction	0.70	0.70
E(LB)	Pascal	Young's Modulus	7.90E+09	7.90E+09
E(PB)*	Pascal	Young's Modulus	7.90E+09	7.90E+09
K(LB)		Krat (*kn/ks*)	2.35	1.00
K(PB)*		Krat (*kn/ks*)	2.35	1.00
Particle size(D_{50})	mm		1.68-2.00	4.00-6.00
LB = Linear bond PB= Parallel Bond				

III.4 Parametric analysis description

The parametric analysis follows the logic presented in **Table 4** where C represents a constant that varies depending on the parameter under the analysis. The parameter's initial value that corresponds to the calibrated value, obtained by fitting the specimen's stress-strain curve with respect to the stress-strain curve of the experimental data is used as the starting point for the parametric analysis. From this value, the constant C is added or subtracted depending on the number of the test. As it is presented in **Table 4**, the initial value is in the middle of the table, being subtracted two times the constant C, for the first test, and one time the constant for the second test. The third test consists of add one-time C, and for the fourth test, it is added two times the constant C.

Table 4. Parameter analysis description.

Parameter = Initial - 2C	Parameter =Initial - C	Initial value	Parameter = Initial + C	Parameter = Initial + 2C

Figure 12 Parametric analysis increment and decrement

In **Table 5**, The initial value is in the middle of the tests, incrementing the value from left to right 1.00 Mpa(C) at every step. The parametric analysis is similar for each parameter. It is designed and prepared depending on the initial value, creating uniform step increments and, using values that allow appreciating the parameters effect on the overall performance.

Table 5. Tensile strength parametric analysis of the mortar cylinder 2D model.

Tensile Strength							
Symbol	Units	Material Properties	T_1.00	T_2.00	Initial	T_4.00	T_5.00
Gap	m	Gap length	2.00E-04	2.00E-04	2.00E-04	2.00E-04	2.00E-04
σ_c	Pascal	Tension strength	1.00E+05	2.00E+05	3.00E+05	4.00E+05	5.00E+05
c	Pascal	Cohesion	3.00E+05	3.00E+05	3.00E+05	3.00E+05	3.00E+05
Φ	Degrees ^{o}	Friction angle	70.00	70.00	70.00	70.00	70.00
μ	-	Particle friction	0.70	0.70	0.70	0.70	0.70
E(LB)	Pascal	Young's Modulus	7.90E+09	7.90E+09	7.90E+09	7.90E+09	7.90E+09
E(PB)	Pascal	Young's Modulus	7.90E+09	7.90E+09	7.90E+09	7.90E+09	7.90E+09
K(LB)	-	Krat (kn/ks)	2.35	2.35	2.35	2.35	2.35
K(PB)	-	Krat (kn/ks)	2.35	2.35	2.35	2.35	2.35
Particle size	mm	-	1.68-2.00	1.68-2.00	1.68-2.00	1.68-2.00	1.68-2.00
LB = Linear bond PB= Parallel Bond							

In **Table 6** parametric analysis of Young's modulus is presented. Each test is carried out at stepping increment of 1.00 GPa, and the results corresponding to each increment are recorded from left to right on the table.

Table 6. E(PB) parametric analysis of the mortar cylinder 2D model

Young's modulus (BPM)							
Symbol	Units	Material Properties	EPB_5.90	EPB_6.90	Initial	EPB_8.90	EPB_9.90
Gap	m	Gap length	2.00E-04	2.00E-04	2.00E-04	2.00E-04	2.00E-04
σ_c	Pascal	Tension strength	3.00E+05	3.00E+05	3.00E+05	3.00E+05	3.00E+05
c	Pascal	Cohesion	3.00E+05	3.00E+05	3.00E+05	3.00E+05	3.00E+05
Φ	Degrees^o	Friction angle	70.00	70.00	70.00	70.00	70.00
μ	-	Particle friction	0.70	0.70	0.70	0.70	0.70
E(LB)	Pascal	Young's Modulus	7.90E+09	7.90E+09	7.90E+09	7.90E+09	7.90E+09
E(PB)	Pascal	Young's Modulus	5.90E+09	6.90E+09	7.90E+09	8.90E+09	9.90E+09
K(LB)	-	Krat (kn/ks)	2.35	2.35	2.35	2.35	2.35
K(PB)	-	Krat (kn/ks)	2.35	2.35	2.35	2.35	2.35
Particle size	mm	-	1.68-2.00	1.68-2.00	1.68-2.00	1.68-2.00	1.68-2.00

LB = Linear bond
PB= Parallel Bond

Parametric analysis for each parameter of the mortar cylinder and concrete block is similarly performed. The tables summarizing the parametric analysis have been presented in **APPENDIX A**.

CHAPTER IV

RESULTS

IV.1 Experiment 1 results

There is a total of 40 simulations that corresponds to the mortar specimens. The cylinder model was simulated 37 times with different combinations of parameters and 3 simulations accounting for different specimen shapes such as the mortar cube 2D, mortar cube 3D, and the mortar cylinder 3D were also done. For the case of the concrete block, a total of 33 simulations were done which includes the simulations done on the initial parameter values.

The following figures summarize the results of the simulations done on mortar composite followed by figures that summarize the results of the simulations on the concrete composite. **Figure 13** shows stress-strain curves obtained when the tensile strength is varied the difference between first test (T=0.10 MPa) and last test (T=0.50 MPa) on the peak stress and its corresponding strain is 62% and 202%, respectively.

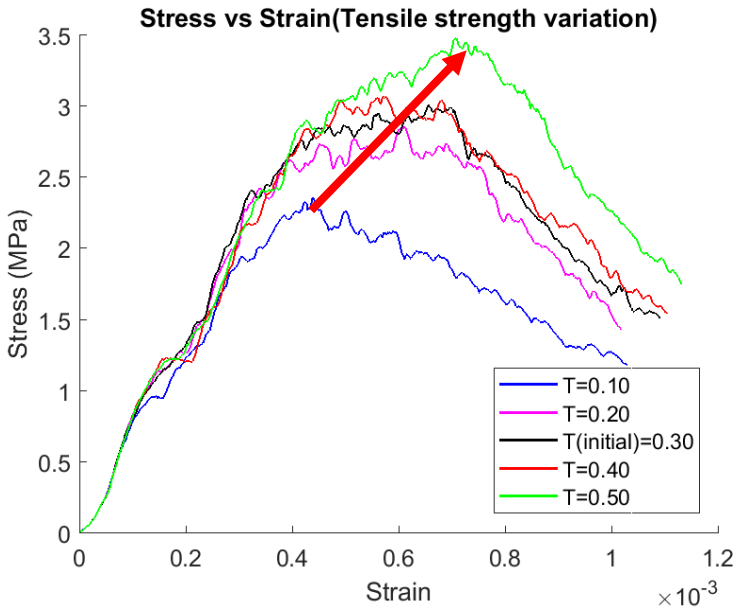

Figure 13.Tensile strength variation stress-strain curves (Mortar cylinder).

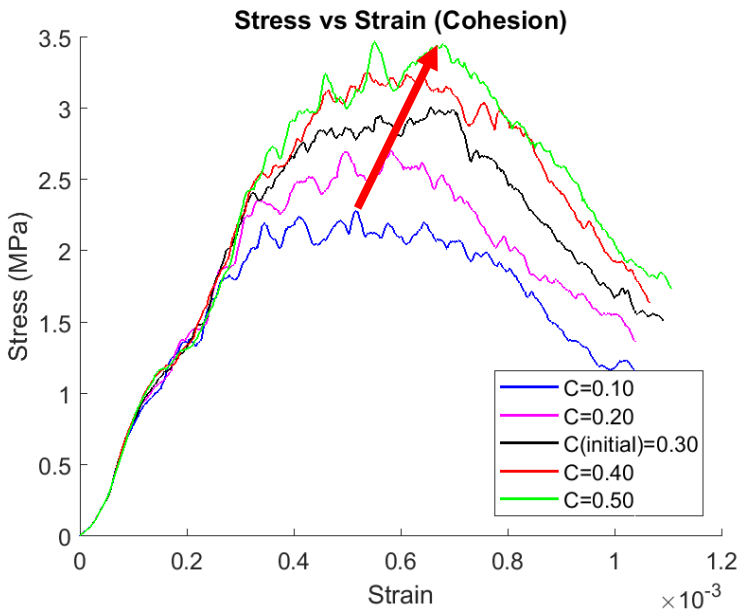

Figure 14. Cohesion variation stress-strain curves (Mortar cylinder).

From **Figure 14** it can be seen that the peak stress of C=0.50 MPa compared with C=0.10 MPa shows a 52% increment. Moreover, a 28% increment with respect to their corresponding strains.

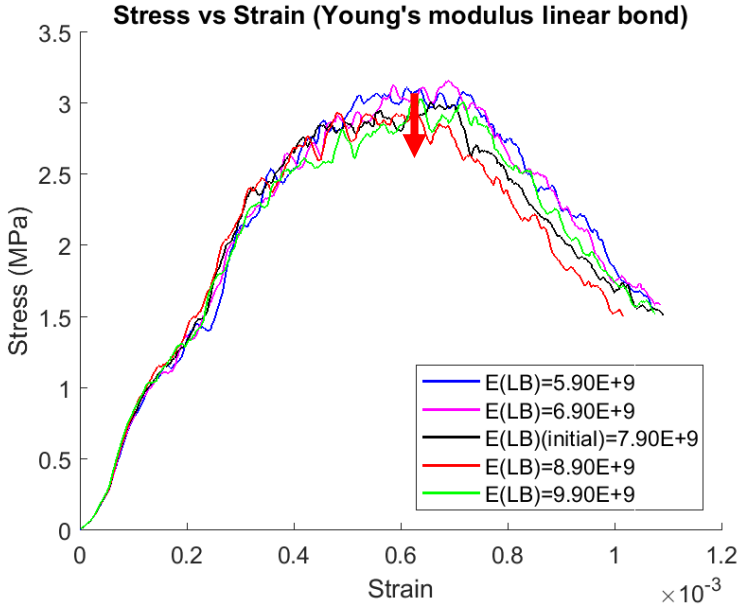

Figure 15. Young's modulus linear bond stress-strain curves (Mortar cylinder).

Figure 15 depicts a 3 % reduction in the peak stress for Young's modulus of the linear model lowest E(LB)=5.90GPa value with the highest one E(LB)=9.90 GPa. The macro Young's modulus of the specimen is not affected significantly when this parameter is modified.

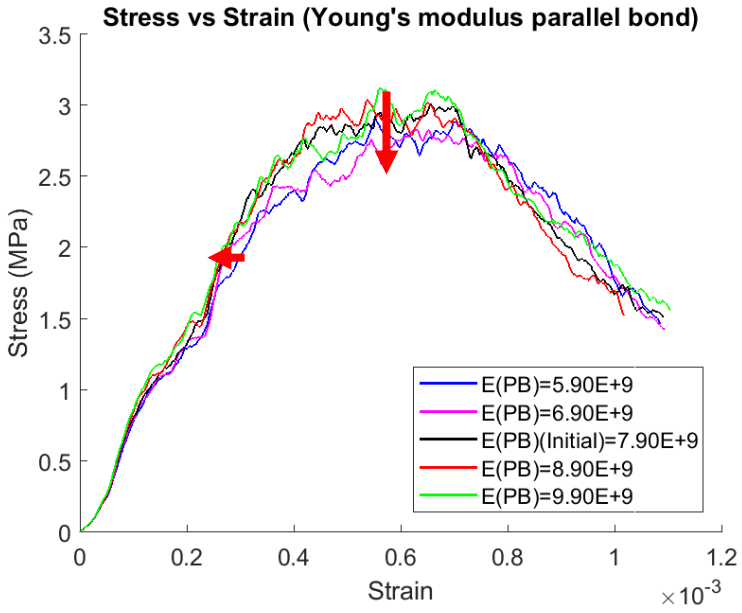

Figure 16. Young's modulus parallel bond stress-strain curves (Mortar cylinder).

In **Figure 16**, a 7% increment in the peak stress can be seen when the lowest Young modulus value for parallel bond EPB=5.90GPa value is compared with the highest value EPB=9.90 GPa. Also, increasing the E(PB) increases the macro Young's modulus of the specimen.

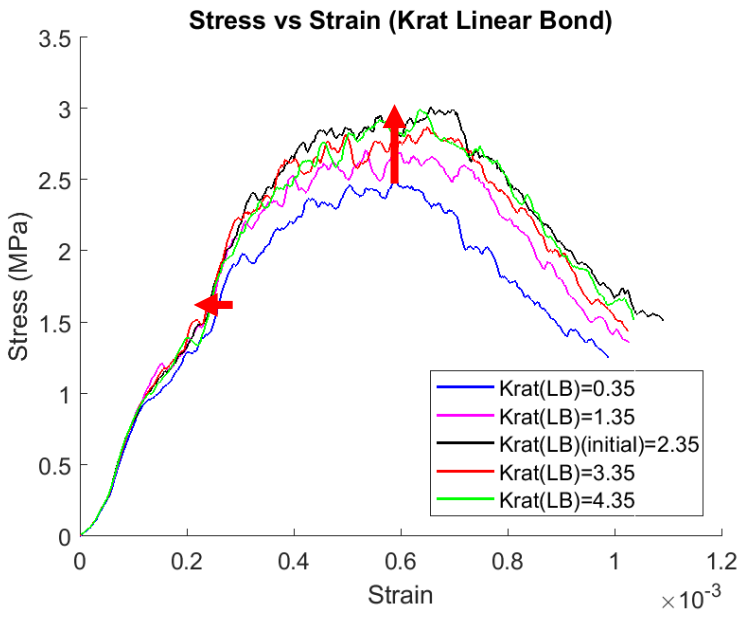

Figure 17. k_n/k_s linear bond stress-strain curves (Mortar cylinder).

From **Figure 17**, the k_n/k_s ratio of the linear model showed a 19% increment on the peak stress comparing the lowest k(LB)=0.35 value with the highest one k(LB)=4.35. Also, the Young Modulus presented an increment when this parameter is increased.

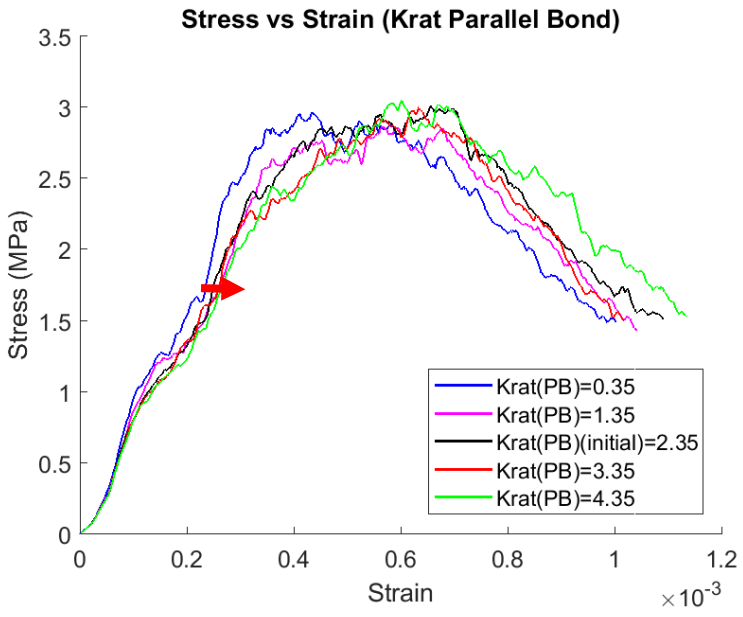

Figure 18. k_n/k_s parallel bond stress-strain curves (Mortar cylinder).

The k_n/k_s ratio of the bonded model, **Figure 18**, showed a 38% increment on the peak stress-strain comparing the lowest k(PB)=0.35 value with the highest one k(PB)=4.35. By modifying the k ratio of the parallel bond, the macro Young's modulus of the specimen increases.

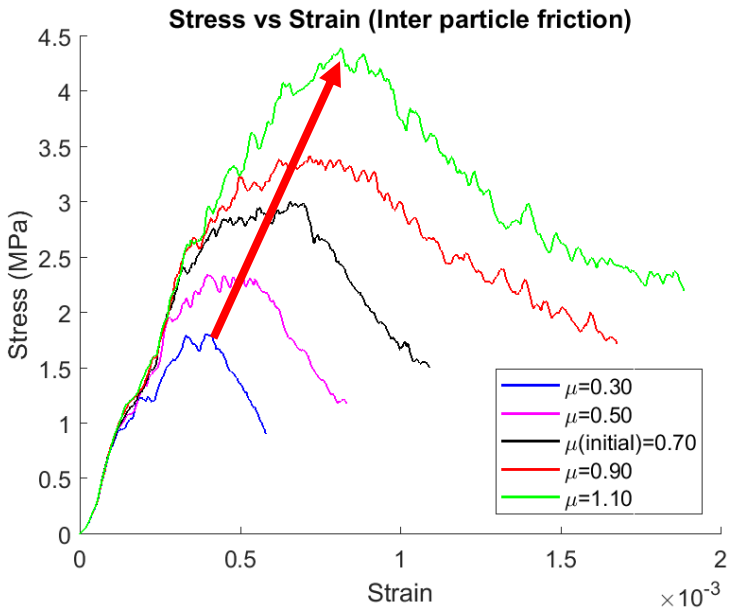

Figure 19. Inter-particle friction coefficient stress-strain curves (Mortar cylinder).

The μ behavior is presented in **Figure 19**. It showed a 240% increment on the peak stress comparing the lowest (μ =0.35) value with the highest one (μ =1.10). Also, their corresponding peak strain shows a 15% increment from the lowest to the highest μ value.

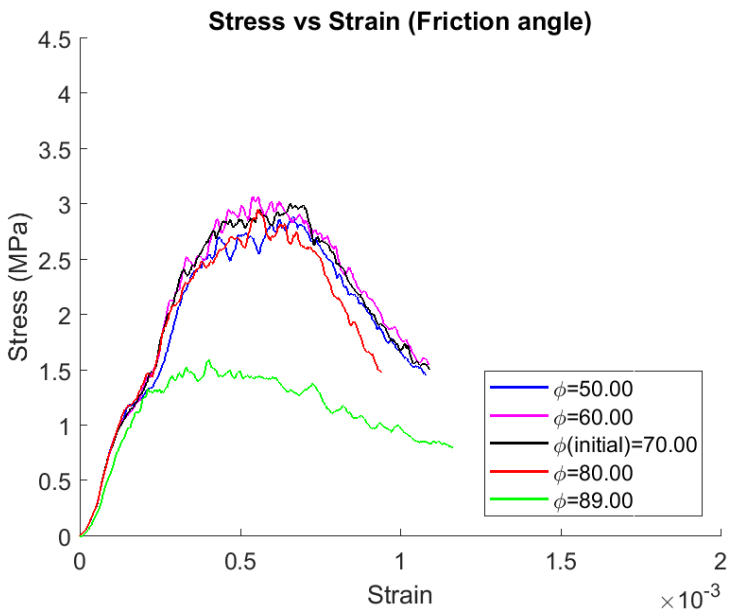

Figure 20. Friction angle stress-strain curves (Mortar cylinder).

In **Figure 20**, the friction angle of the bonded model showed a 35% decrease in the strain corresponding to the peak stress comparing the lowest Φ=5 with the highest Φ=89. From Φ = 50-80 peak stress their corresponding strain seem to be consistent. Φ = 89 is an extreme value and showed a sudden drop in the strength of the material.

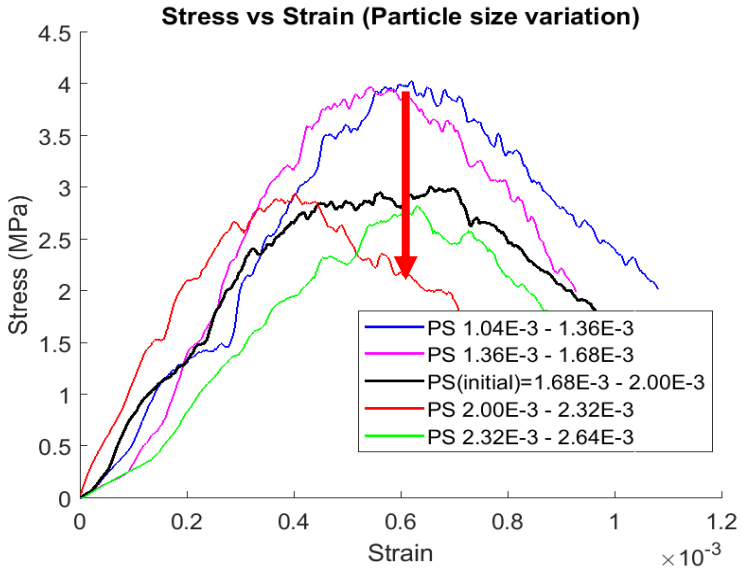

Figure 21. Particle size stress-strain curves. (mortar cylinder)

The particle size (**Figure 21**) showed a 142% decrease of the peak stress when the particle size compares the lowest particles' diameter (PS=1.04-1.36 E-3) to the highest (PS= 2.32-2.64 E-3).

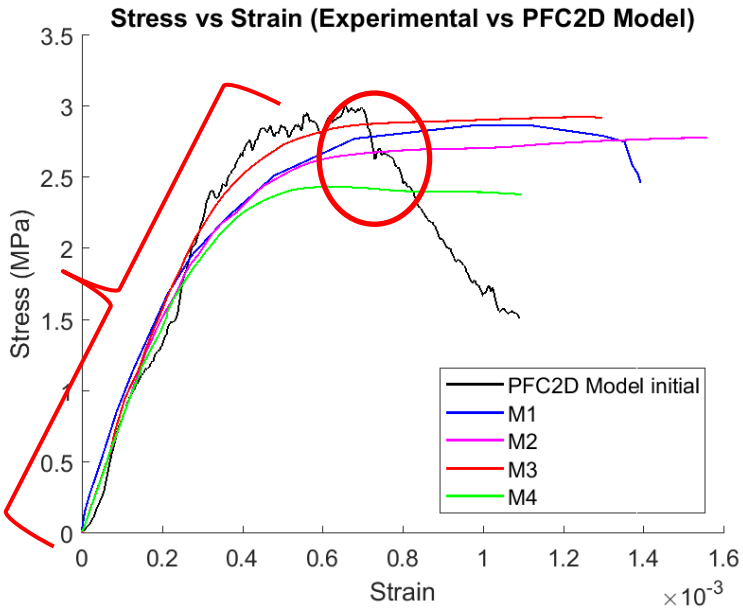

Figure 22. Experimental data vs. PFC2D

The initial parameters' values used for the parameters analysis is shown in **Figure 22**. In this figure the lines from M1 – M4 correspond to the experimental observations. The black line called PFC2D is the DEM simulation with the parameters' combination that represents closer the experimental observations. It is possible to observe that the model can represent the elastic section of the experimental observations. Nonetheless, the behavior is more brittle compared with the experimental data.

Mortar cylinder simulation is presented in four stages in **Figure 23** and **Figure 24**. The first stage no load has been applied to the sample. The second stage is the initial part of the Unconfined Compression Test. The third stage shows when the peak stress is reached. The fourth and final stage is when the UCT has stopped.

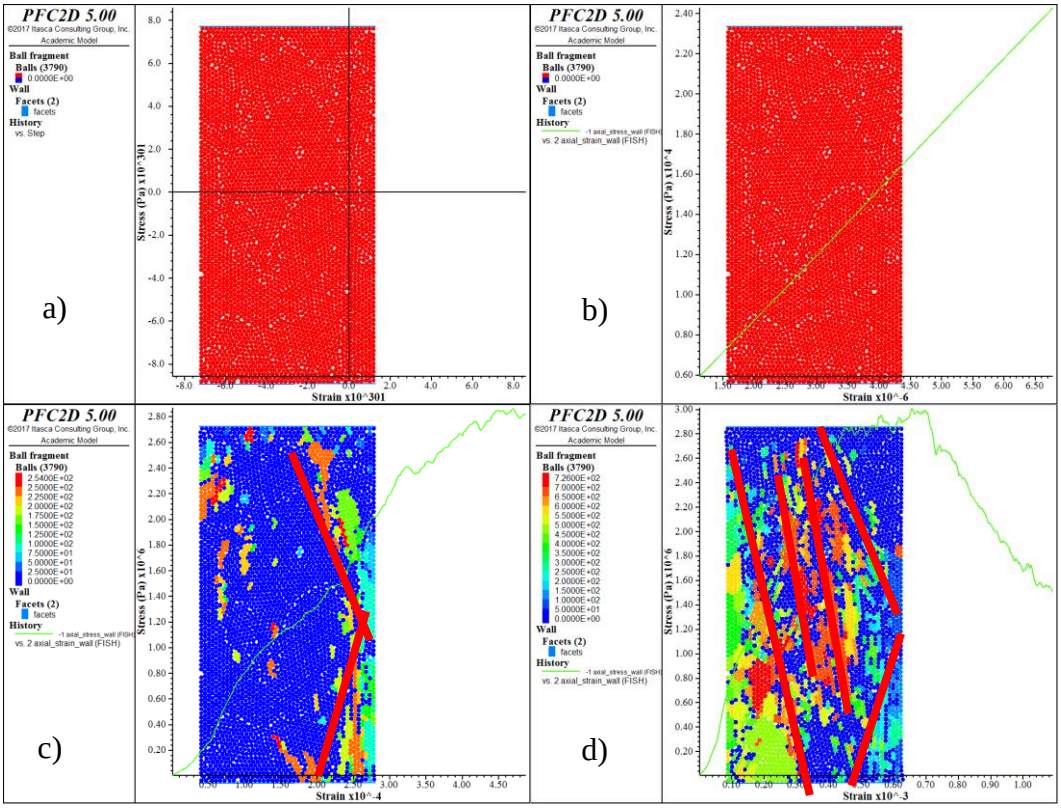

Figure 23. Fracture of Unconfined compression test of the initial parameters' values of the mortar cylinder DEM.

The colors in **Figure 23** represent the number of balls of the fragmented particles. Also, the particles change of color by order of appearance in time. **Figure 23**(c) shows first shear bands. **Figure 23**(d) the final crack pattern is shown. At this stage, the left bottom section shows a considerable cracking. Red lines in the figure mark the principal crack patterns.

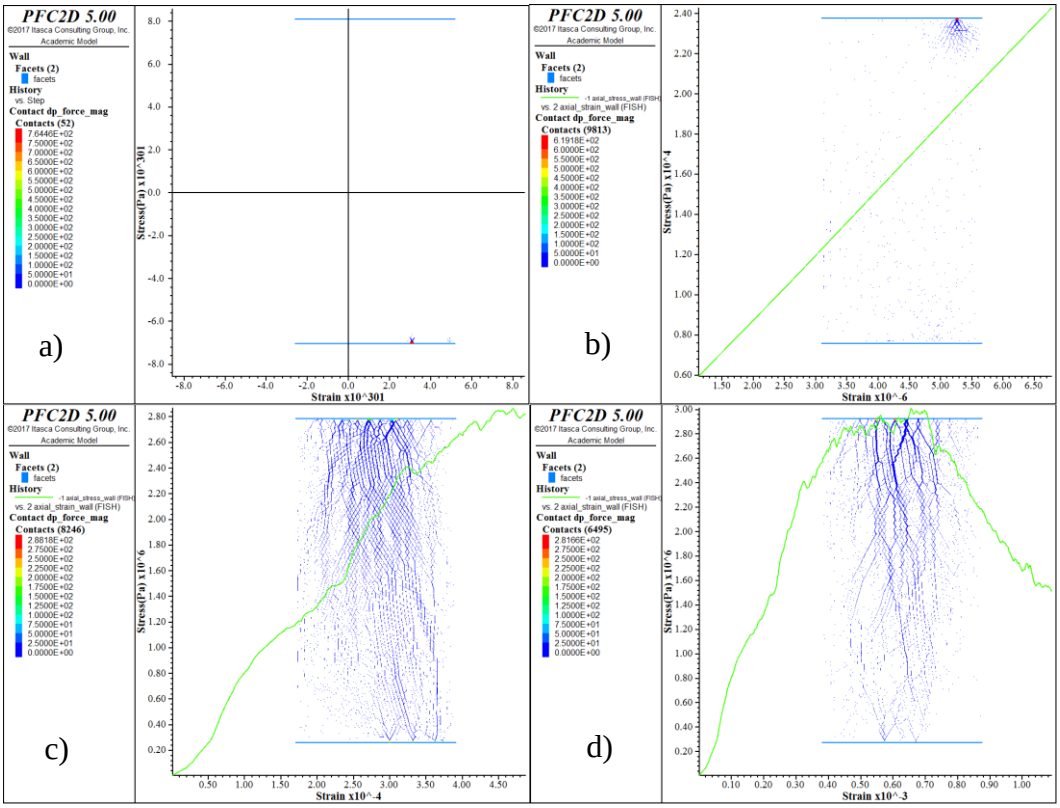

Figure 24. Contact forces of Unconfined compression test of the initial parameters' values of the mortar cylinder DEM.

Figure 24 presents the contact forces at same stages as **Figure 23**. Thicker lines represent more contact force magnitude. At stage 1 **Figure 24**(a) there are no contact forces because UCT has not started. **Figure 24**(b) contact forces started to present. **Figure 24**(c) contact forces are concentrated at the top center of the specimen. **Figure 24**(d) contact forces have diminished due to the increment of fragmentation.

IV.1.1 **Experiment 1 observations**

The tensile strength, cohesion, and inter-particle friction coefficient are the parameters that affect the most the specimens' peak stress. Refer to **Figure 13, Figure 14, and Figure 19**. It is

possible to see this effect with the red arrows. The inter-particle friction coefficient showed the most influence on the peak stress. The interparticle coefficient showed 240% increment of the peak stress compared with the 52% increment showed by the tensile and cohesive strength. The increment of the parameters is 366%, 500%, and 500% corresponding to the interparticle friction angle, cohesive and tensile strength respectively.

The friction angle at an extreme value such as 89° showed a sudden decrease on the specimen's peak stress. It is related to the coulomb limit imposed in the shear strength. The coulomb formula does not take 90° as a friction angle value.

Young's modulus (PB) and k(PB) presented most influence on the overall specimen's Young's modulus. Refer to Figure 16 and Figure 18.

Particle size changes the peak stress resistance on the model. This phenomenon is because of the more particles, the more contacts. Therefore, more contacts with the same parameters values, the model resists more the disturbances caused by same loading scenario.

IV.2 Experiment 2 results

In **Figure 25** a comparison between the different geometries and approaches of the model is presented. The cylindrical and cubic model of the mortar, using a 2D and 3D approach is reviewed.

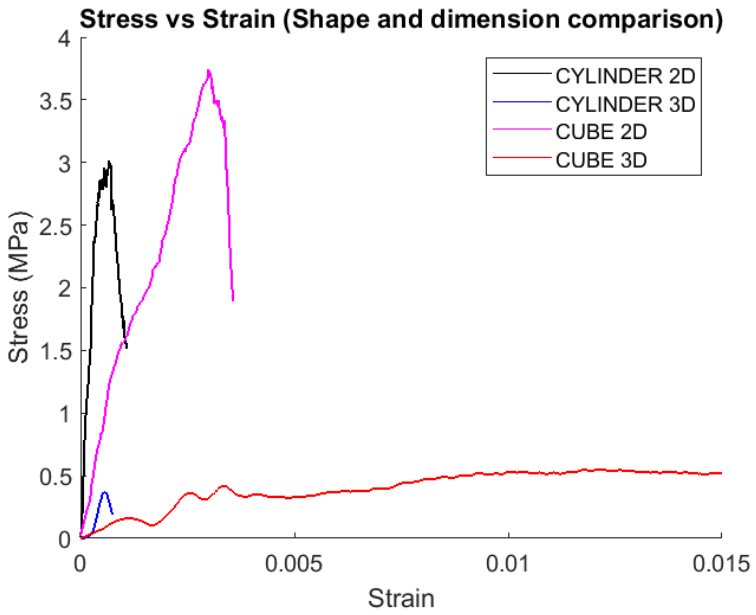

Figure 25. Shape and dimension comparison of the mortar.

IV.2.1 **Experiment 2 observations**

Mortar calibrated parameters' showed accuracy when predicting peak stress on the 2D approach for the cylinder and cube.

Initial calibration on the 3D approach for the mortar cylinder and cube did not show the expected behavior of the stress-strain curve. The assumption of 2D particles is that particles are considered as a cylinder of unit thickness with a diameter of the particle diameter. Compared with the spherical shape produced in the 3D assumption[32]. Therefore, this assumption might affect the model behavior.

IV.3 Experiment 3 results

The following figures review the concrete block simulations when its parameters are varied.

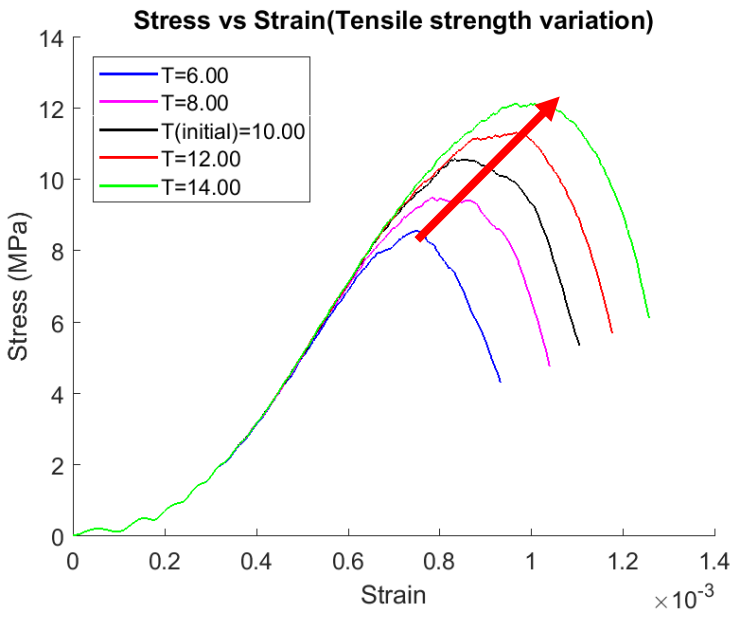

Figure 26. Tensile strength stress-strain curves (Concrete block)

Figure 26 the difference between first tensile strength test (T= 6.00 MPa) and last test (T=14.00 MPa) on the peak stress and its corresponding strain is 62% and 57%, respectively.

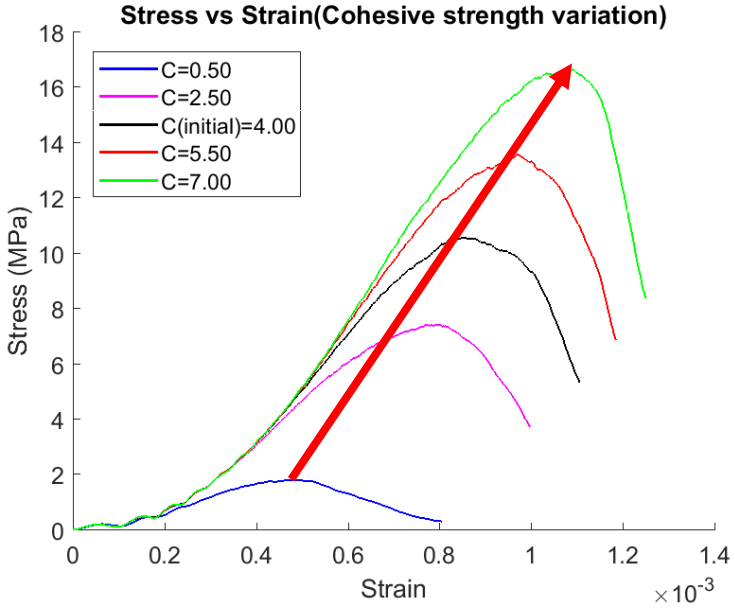

Figure 27. Cohesive strength stress-strain curves (concrete block).

Cohesive strength variation in **Figure 27**, the peak stress of C=0.50 MPa compared with C=7.00 MPa shows 800% increment. Corresponding strain at peak stresses increases 240%. When comparing from C= 2.50 MPa to C = 7.00 Mpa there is a 242% increment on the peak stress and 37% increment on their corresponding strains.

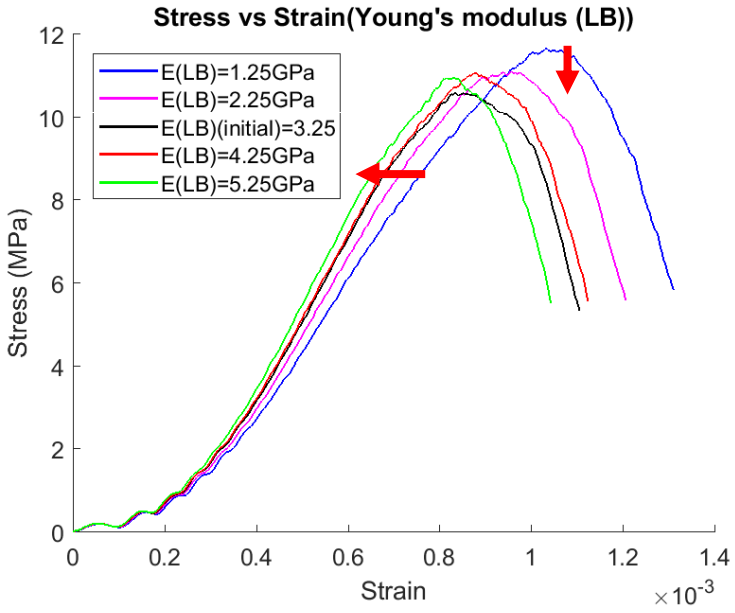

Figure 28. Young's modulus linear bond stress-strain curves (concrete block).

In **Figure 28**, the difference of E(LB) = 1.25 peak stress's strain with respect to E(PB) = 5.25 is 31% decrease. The peak stresses showed a 4% decrease. It also showed a variation on the slope meaning a variation on Young's modulus.

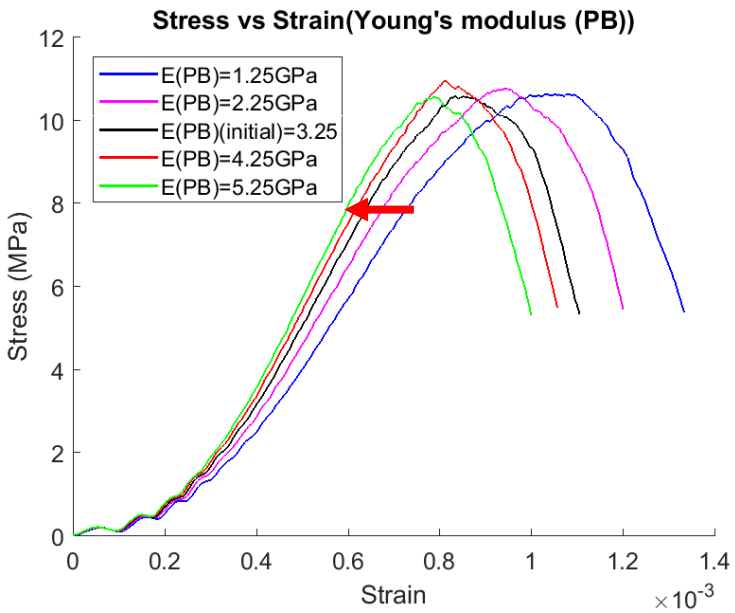

Figure 29. Young's modulus parallel bond stress-strain curves (concrete block)

In **Figure 29**, the difference of E(PB) = 1.25 peak stress's strain with respect to E(PB) = 5.25 is 28% decrease. The peak stress did not show a considerable change. The Young's modulus increased when the E(PB) is increased.

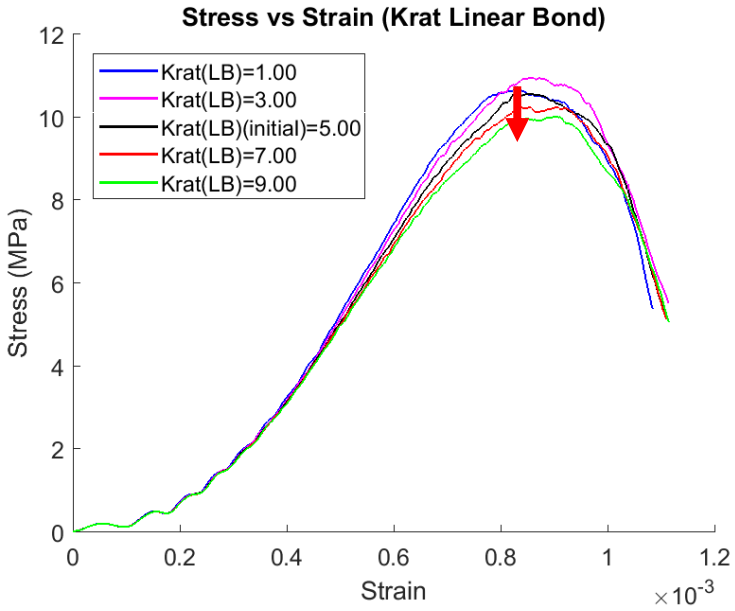

Figure 30. k_n/k_s linear bond stress-strain curves (concrete block)

Figure 30 exhibits a 16 % decrease when comparing k(LB) = 1.00 peak stress with respect to E(LB) = 9.00. The corresponding strain for the peak stresses increases 12%.

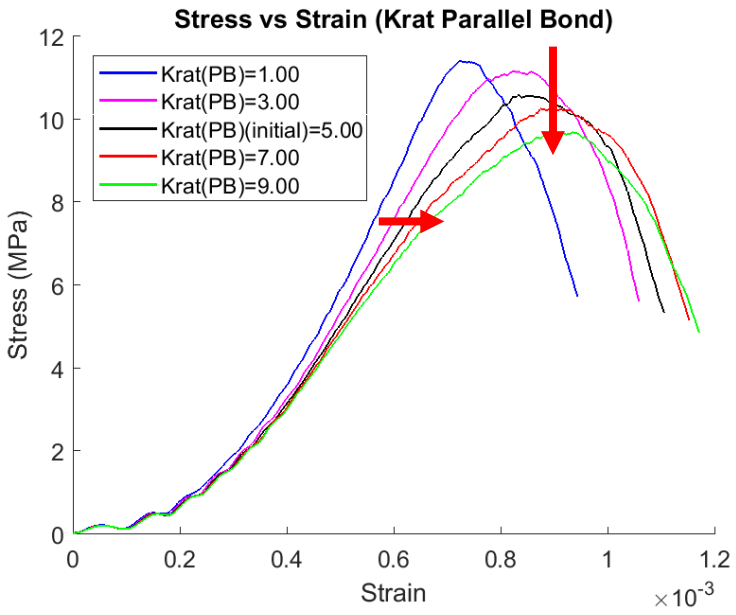

Figure 31. k_n/k_s parallel bond stress-strain curves (concrete block)

From **Figure 31**, the difference of k(LB) = 1.00 peak stress with respect to E(LB) = 9.00 is 28% decrease. Their corresponding strains showed an increase of 28%. The Young's modulus of the specimen is reduced when this value is increased.

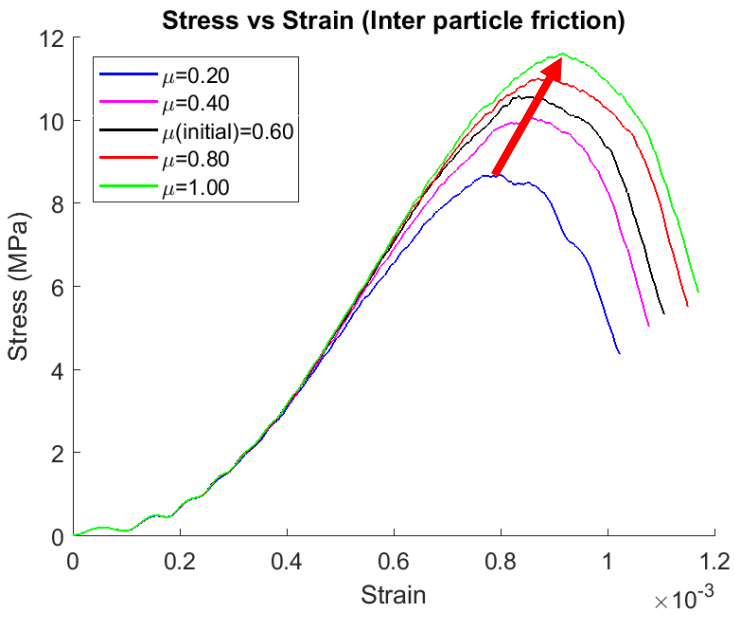

Figure 32. Interparticle friction coefficient stress-strain curves (concrete block)

The interparticle friction presented in **Figure 32**, shows an increase of 50% when comparing μ= 0.20 peak stress with respect to μ= 1.00. Their corresponding strain displayed 28% increase.

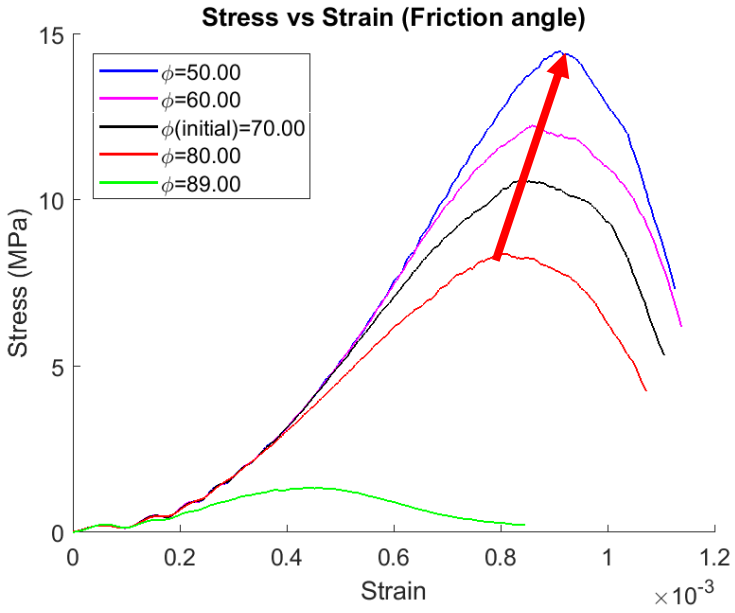

Figure 33. Friction angle stress-strain curves (concrete block)

From **Figure 33**, the friction angle showed a 187% decrease in the peak stress when it goes from 50 to 80. Moreover, a 28% decrease in their corresponding strains. Comparing Φ = 50 to an extreme value of Φ = 89 (being Φ =90° not acceptable by Mohr-Coulomb theory) the modeled showed a 750% reduction on the peak stress and 80% decrease on their corresponding strains.

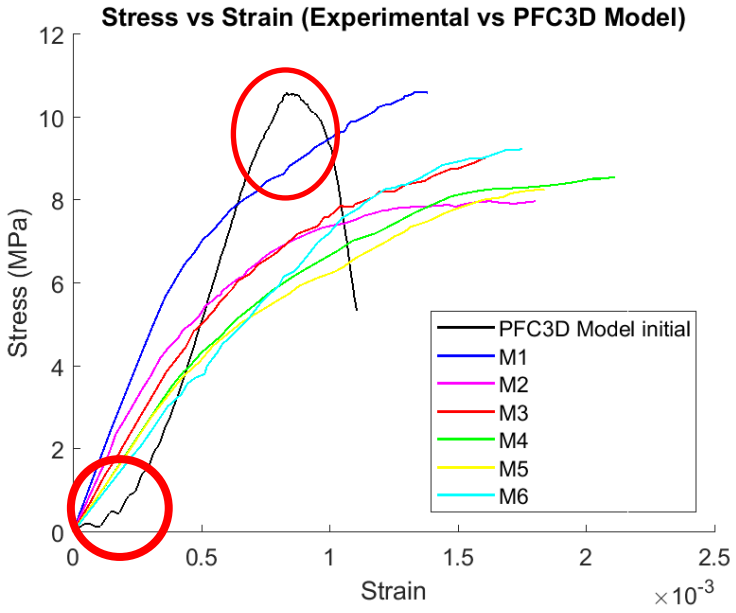

Figure 34. PFC3D simulation vs experimental data.

The model of the concrete block showed to be more brittle compared to the experimental observations, refer to **Figure 34**. Also, the model initial section presented particle accommodation creating noise at initial data.

Figure 35 and **Figure 36** show four stages of the concrete block simulation. First, no load applied, the second beginning of the UCT, third when peak stress has reached, and fourth is a final cracking stage when the UCT is stopped.

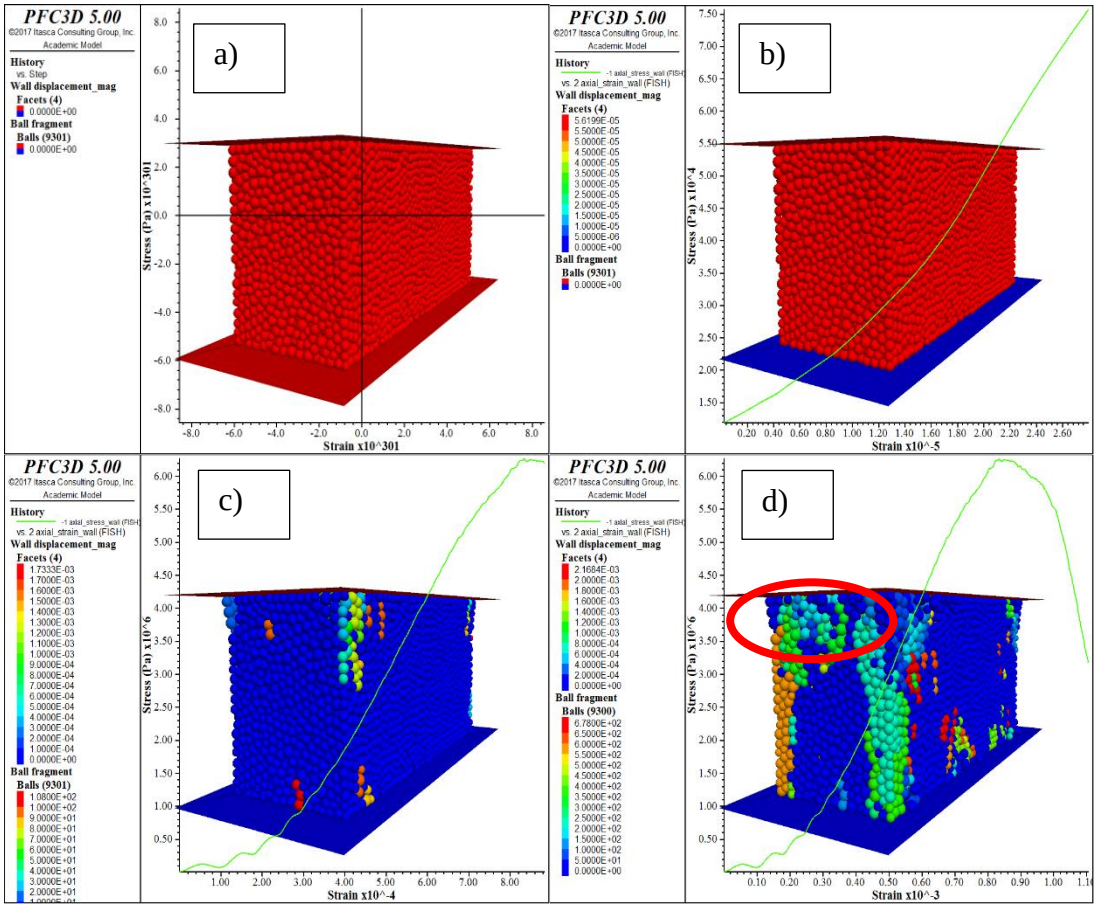

Figure 35. Fracture of Unconfined compression test of the initial parameters' values of the concrete block DEM.

In **Figure 35** (a) the model does not show any crack similar to **Figure 35** (b) at first stage. **Figure 35** (c) shows cracking initiation. **Figure 35** (d) shows the final stage where the corner of the concrete block is fractured and particles in red circle show initial detachment.

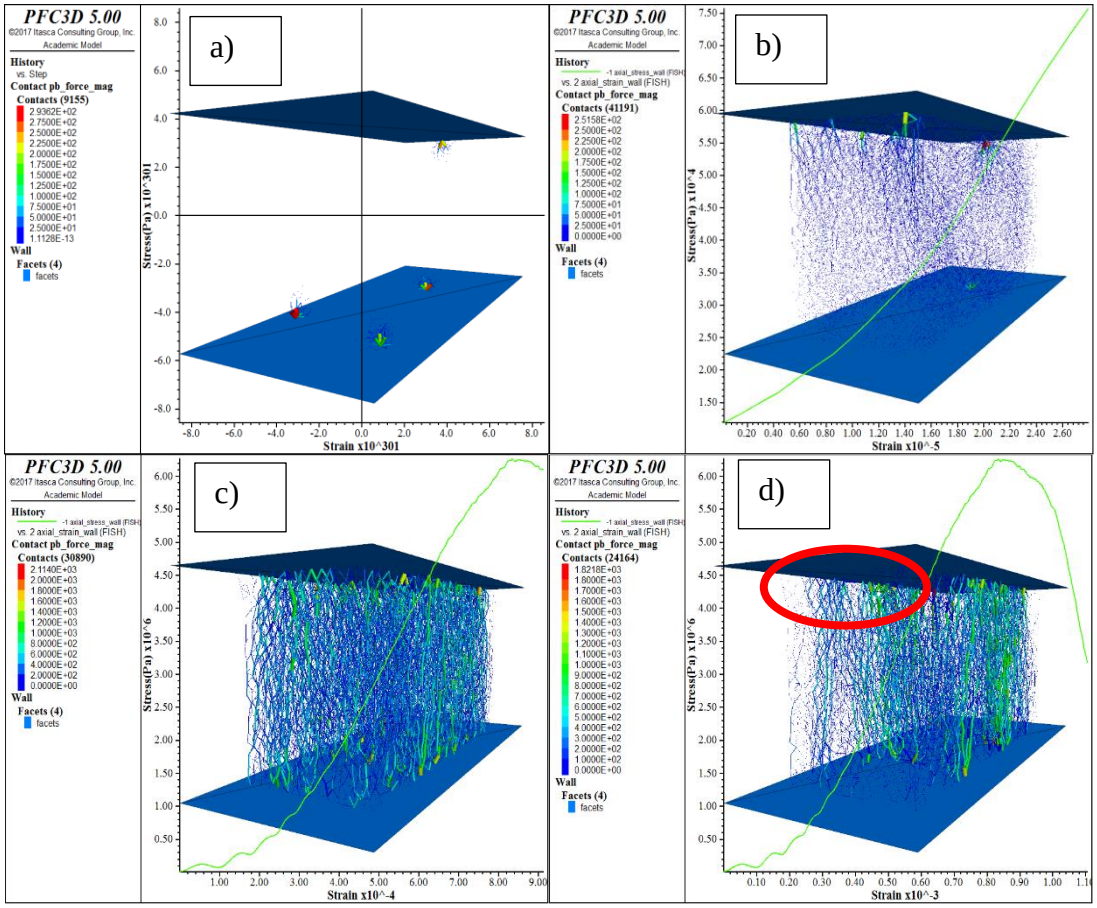

Figure 36. Contact forces of Unconfined compression test of the initial parameters' values of the concrete block DEM.

Contact forces start presenting when the test is occurring. In **Figure 36**(b) contact forces are minimized. **Figure 36**(c) contact forces are all over the sample and **Figure 36**(d contact forces has diminished due to cracking. The underlined red circle shows that there are no contact forces when particles detach.

IV.3.1 **Experiment 3 observations**

The tensile strength, cohesion, and inter-particle friction coefficient are the parameters that affect the most the specimen's peak stress. The interparticle friction increased 800% when the

tensile strength value increased 1400%. This presented comparison shows that this parameter is the one that affects the most the peak stress. The tensile strength and the cohesion changed 233% and 500% with increments on their peak stresses corresponding to 57% and 50% respectively.

When friction angle's value increases, the peak stress decreases. The friction angle at an extreme value such as 89° will show a sudden decrease in the specimen's peak stress. AS explained this is because it is imposed a coulomb limit on the shear strength. The coulomb laws cannot take friction angle as 90°.

Kratio(PB), E(PB) and E(LB) are the parameters that affect the most the specimen's Young modulus. Refer to **Figure 28, Figure 29, and Figure 31.**

CHAPTER V

CONCLUSIONS

The Discrete Element Models were not able to adequately represent the mechanical behavior of a Concrete block and a mortar cylinder under compression test.

When comparing the results from the mortar cylinder with the cube, it is possible to see that geometry influence in the mechanical behavior.

Scaling (2D and 3D) of the model showed inconsistency by comparing results of the mortar cube and mortar cylinder. Therefore it is necessary to consider the correct approach depending on the model geometry.

The concrete block DEM does not represent the experimental data. Therefore, the usage of another constitutive model should be considered.

Since calibration was not fulfilled in both specimens, it is recognized that another calibration procedure should be used. It is proposed to use a probabilistic calibration which can be capable of examining all possible scenarios and parameter's combinations that fit the experimental observations.

Probabilistic calibration is capable of showing the parameter's correlation. Therefore, this procedure brings a more in-depth analysis of the parameters' influence on the specimen mechanical behavior.

REFERENCES

[1] P. G. Asteris, Plevris and V. Plevris, "Numerical Modeling of Historic Masonry Structures," in *Seismic Assessment and Rehabilitation of Historic Structures*, I. GLOBAL, Ed., 2015.

[2] S. M. Alcocer *et al.*, "Seguridad Sismica de la Vivienda Economica," 1994.

[3] E. Çakti *et al.*, "Discrete element modeling of a scaled masonry structure and its validation," *Engineering Structures*, p. 13, 2016.

[4] J. N. Reddy, J. J. Corrigan and J. M. Morris, Eds. *An Introduction to the finite Element Method*, Second ed. McGraw-Hill, Inc, 1993.

[5] A. Stavridis and P. B. Shing, "Finite-Element Modeling of Nonlinear Behavior of Masonry-Infilled RC Frames," *Journal Of Structural Engineering © ASCE*, 2010.

[6] J. A. Campbell Barraza, "Numerical Model for Nonlinear Analysis of Masonry Walls," Doctor of Philosophy, RWTH Aachen University, 2012.

[7] J. F. Lizárraga and J. J. Pérez Gavilán, "Nonlinear Modelling Of Masonry Walls Using Contact Elements (Modelación No Lineal De Muros De Mampostería Empleando Elementos De Contacto)," *Revista de Ingeniería Sísmica No. 93 41-59 (2016)*, 2015.

[8] P. B. Laurenco, "Computational Strategies For Masonry Structures," Doctor of Philosophy Civil Engineering, Delft University of Technology, Netherlands, 1996.

[9] M. A. Gonzalez Herrera, "Comportamiento De La Mampostería De Bloques Huecos De Concreto De Distintos Espesores, Sujeta A Compresión Axial," Master of Science Civil Engineering, Universidad Autonoma de Yucatan, Mexico, 2010.

[10] B. R. Indriyantho and Nuroji, "Finite element modeling of concrete fracture in tension with the Brazilian splitting test on the case of plane-stress and plane-strain," *Procedia engineering*, 2014.

[11] A. Thavalingam *et al.*, "Computational framework for discontinous modelling of masonry arch bridges," *Computers and Structures*, 2001.

[12] V. Sarhosis *et al.*, "A review of experimental investigations and assessment methods for masonry arch bridges," *Structure and Infrastructure Engineering*, 2016.

[13] A. Munjiza, *The Combined Finite-Discrete Element Method*. England: John Wiley and Sons, LTD, 2004.

[14] S. Hrvoje *et al.*, "A combined finite–discrete numerical model for analysis of masonry structures," *Engineering Fracture Mechanics*, 2014.

[15] H. Smoljanovic *et al.*, "A combined finite-discrete element analysis of dry stone masonry structures," *Engineering Structures*, 2013.

[16] Y. S. Erdogan *et al.*, "Seismic analysis and investigation of damage mechanism of 57th infantry regiment memorial using finite-discrete element method," *Bull Earthquake Eng*, 2015.

[17] H. Smoljanovic *et al.*, "Numerical analysis of 3D dry-stone masonry structures by combined finite-discrete element method," *International Journal of Solids and Structures*, 2017.

[18] Y. P. Yuen and J. S. Kuang, "Masonry-Infilled Rc Frames Subjected To Combined In-Plane And Out-Of-Plane Loading," *International Journal of Structural Stability and Dynamics*, vol. 2, no. 2, p. 17, 2014.

[19] A. Munjinza *et al.*, "Combined single and smeared crack model in combined Finite-Discrete Element analysis," *International Journal for Numerical Methods in Engineering*, p. 44, 1999.

[20] P. A. Cundall and O. D. L. Strack, "A Discrete Numerical Model for Granular Assemblies," *Geotechnique*, pp. 45-65, 1979.

[21] V. Sarhosis *et al.*, "Distinct Element Modelling of Masonry Wall Panels with Openings," *Proceedings of The Ninth Iinternational Conference on Computational Structures Technology*, 2008.

[22] C. G. I. Itasca, "PFC Version 5.0 documentation," ed. Minneapolis, MN, USA, 2017.

[23] A. Isfeld and N. Shrive, "Discrete Element Modeling of Stone Masonry Walls With Varying Core Conditions: Prince of Wales Fort Case Study," *International Journal of Architectural Heritage*, 2015.

[24] M. Watters, "A Study of the Influence of Particle Gradation in Bonded Assemblies," Undergraduate thesis, Civil Engineering, University of Arkansas, Fayetteville, AR, 2015.

[25] Z. Gyurko and A. Borosnyoi, "Brinell-hardness testing and discrete element modelling of hardened concrete," *Journal of Silicate Based and Composite Materials*, vol. 67, 2015.

[26] J. D. Riera *et al.*, "Assessment of Brazilian tensile test by means of the truss-like Discrete Element Method (DEM) with imperfect mesh," *Engineering Structures*, 2014.

[27] T. Ulrich *et al.*, "Using the discrete element method to assess the seismic vulnerability of aggregated masonry buildings," *Bulletin of Earthquake Engineering*, 2014.

[28] J. Hernandez Santillan, "Comportamiento No Lineal De La Mampostería De Bloques Huecos De Concreto Sujeta A Compresión Axial," Master of Science, Civil Engineering, Universidad Autonoma de Yucatan, Merida, Mexico, 2015.

[29] M. F. Ortiz Cahun, "Comportamiento de un muro de mamposteria rehabilitado, sujeto a cargas laterales. ," Bachelor, Universidad Autonoma de Yucatan, Merida, Yucatan, Mexico, 2014.

[30] Y. Zhang, "Probabilistic Calibration of a Discrete Particle Model," Master of Science, Civil Engineering, Texas A&M University, 2010.

[31] D. O. Potyondy and P. A. Cundall, "Abonded-particle model for rock," *International Journal of Rock Mechanics & Mining Sciences*, 2004.

[32] D. O. Potyondy, "Material-Modeling Support in PFC," in *PFC 5 Documentation Set*, 2017.

APPENDIX A

This appendix presents all parametric combination tables that were used in this work.

Mortar cylinder 2D parametric analysis tables are presented.

			Tensile Strength(mortar)				
Symbol	Units	Material Properties	T_1.00	T_2.00	Initial	T_4.00	T_5.00
Gap	m	Gap length	2.00E-04	2.00E-04	2.00E-04	2.00E-04	2.00E-04
σ_c	Pascal	Tension strength	1.00E+05	2.00E+05	3.00E+05	4.00E+05	5.00E+05
c	Pascal	Cohesion	3.00E+05	3.00E+05	3.00E+05	3.00E+05	3.00E+05
Φ	Degrees^o	Friction angle	70.00	70.00	70.00	70.00	70.00
μ	-	Particle friction	0.70	0.70	0.70	0.70	0.70
E(LB)	Pascal	Young's Modulus	7.90E+09	7.90E+09	7.90E+09	7.90E+09	7.90E+09
E*(PB)	Pascal	Young's Modulus	7.90E+09	7.90E+09	7.90E+09	7.90E+09	7.90E+09
K(LB)	-	Krat (kn/ks)	2.35	2.35	2.35	2.35	2.35
K*(PB)	-	Krat (kn/ks)	2.35	2.35	2.35	2.35	2.35
Particle size	mm	-	1.68-2.00	1.68-2.00	1.68-2.00	1.68-2.00	1.68-2.00

LB = Linear bond
PB= Parallel Bond

			Cohesion (mortar)				
Symbol	Units	Material Properties	C_1.00	C_2.00	Initial	C_4.00	C_5.00
Gap	m	Gap length	2.00E-04	2.00E-04	2.00E-04	2.00E-04	2.00E-04
σ_c	Pascal	Tension strength	3.00E+05	3.00E+05	3.00E+05	3.00E+05	3.00E+05
c	Pascal	Cohesion	1.00E+05	2.00E+05	3.00E+05	4.00E+05	5.00E+05
Φ	Degrees^o	Friction angle	70.00	70.00	70.00	70.00	70.00
μ	-	Particle friction	0.70	0.70	0.70	0.70	0.70
E(LB)	Pascal	Young's Modulus	7.90E+09	7.90E+09	7.90E+09	7.90E+09	7.90E+09
E*(PB)	Pascal	Young's Modulus	7.90E+09	7.90E+09	7.90E+09	7.90E+09	7.90E+09
K(LB)	-	Krat (kn/ks)	2.35	2.35	2.35	2.35	2.35
K*(PB)	-	Krat (kn/ks)	2.35	2.35	2.35	2.35	2.35
Particle size	mm	-	1.68-2.00	1.68-2.00	1.68-2.00	1.68-2.00	1.68-2.00

LB = Linear bond
PB= Parallel Bond

			E(PB)				
Symbol	Units	Material Properties	EPB_5.90	EPB_6.90	Initial	EPB_8.90	EPB_9.90
Gap	m	Gap length	2.00E-04	2.00E-04	2.00E-04	2.00E-04	2.00E-04
σ_c	Pascal	Tension strength	3.00E+05	3.00E+05	3.00E+05	3.00E+05	3.00E+05
c	Pascal	Cohesion	3.00E+05	3.00E+05	3.00E+05	3.00E+05	3.00E+05
Φ	Degrees^o	Friction angle	70.00	70.00	70.00	70.00	70.00
μ	-	Particle friction	0.70	0.70	0.70	0.70	0.70
E(LB)	Pascal	Young's Modulus	7.90E+09	7.90E+09	7.90E+09	7.90E+09	7.90E+09
E*(PB)	Pascal	Young's Modulus	5.90E+09	6.90E+09	7.90E+09	8.90E+09	9.90E+09
K(LB)	-	Krat (kn/ks)	2.35	2.35	2.35	2.35	2.35
K*(PB)	-	Krat (kn/ks)	2.35	2.35	2.35	2.35	2.35
Particle size	mm	-	1.68-2.00	1.68-2.00	1.68-2.00	1.68-2.00	1.68-2.00

LB = Linear bond
PB= Parallel Bond

			E(LB)				
Symbol	Units	Material Properties	ELB_5.90	ELB_6.90	Initial	ELB_8.90	ELB_9.90
Gap	m	Gap length	2.00E-04	2.00E-04	2.00E-04	2.00E-04	2.00E-04
σ_c	Pascal	Tension strength	3.00E+05	3.00E+05	3.00E+05	3.00E+05	3.00E+05
c	Pascal	Cohesion	3.00E+05	3.00E+05	3.00E+05	3.00E+05	3.00E+05
Φ	Degrees ^{o}	Friction angle	70.00	70.00	70.00	70.00	70.00
μ	-	Particle friction	0.70	0.70	0.70	0.70	0.70
E(LB)	Pascal	Young's Modulus	5.90E+09	6.90E+09	7.90E+09	8.90E+09	9.90E+09
E*(PB)	Pascal	Young's Modulus	7.90E+09	7.90E+09	7.90E+09	7.90E+09	7.90E+09
K(LB)	-	Krat (kn/ks)	2.35	2.35	2.35	2.35	2.35
K*(PB)	-	Krat (kn/ks)	2.35	2.35	2.35	2.35	2.35
Particle size	mm	-	1.68-2.00	1.68-2.00	1.68-2.00	1.68-2.00	1.68-2.00

LB = Linear bond
PB= Parallel Bond

			Friction angle				
Symbol	Units	Material Properties	FA_50	FA_60	Initial	FA_80	FA_90
Gap	m	Gap length	2.00E-04	2.00E-04	2.00E-04	2.00E-04	2.00E-04
σ_c	Pascal	Tension strength	3.00E+05	3.00E+05	3.00E+05	3.00E+05	3.00E+05
c	Pascal	Cohesion	3.00E+05	3.00E+05	3.00E+05	3.00E+05	3.00E+05
Φ	Degrees^o	Friction angle	50.00	60.00	70.00	80.00	89.00
μ	-	Particle friction	0.70	0.70	0.70	0.70	0.70
E(LB)	Pascal	Young's Modulus	7.90E+09	7.90E+09	7.90E+09	7.90E+09	7.90E+09
E*(PB)	Pascal	Young's Modulus	7.90E+09	7.90E+09	7.90E+09	7.90E+09	7.90E+09
K(LB)	-	Krat (kn/ks)	2.35	2.35	2.35	2.35	2.35
K*(PB)	-	Krat (kn/ks)	2.35	2.35	2.35	2.35	2.35
Particle size	mm	-	1.68-2.00	1.68-2.00	1.68-2.00	1.68-2.00	1.68-2.00

LB = Linear bond
PB= Parallel Bond

			K Ratio(PB)				
Symbol	Units	Material Properties	KPB_0.35	KPB_1.35	Initial	KPB_3.35	KPB4.35
Gap	m	Gap length	2.00E-04	2.00E-04	2.00E-04	2.00E-04	2.00E-04
σ_c	Pascal	Tension strength	3.00E+05	3.00E+05	3.00E+05	3.00E+05	3.00E+05
c	Pascal	Cohesion	3.00E+05	3.00E+05	3.00E+05	3.00E+05	3.00E+05
Φ	Degrees^o	Friction angle	70.00	70.00	70.00	70.00	70.00
μ	-	Particle friction	0.70	0.70	0.70	0.70	0.70
E(LB)	Pascal	Young's Modulus	7.90E+09	7.90E+09	7.90E+09	7.90E+09	7.90E+09
E*(PB)	Pascal	Young's Modulus	7.90E+09	7.90E+09	7.90E+09	7.90E+09	7.90E+09
K(LB)	-	Krat (kn/ks)	2.35	2.35	2.35	2.35	2.35
K*(PB)	-	Krat (kn/ks)	0.35	1.35	2.35	3.35	4.35
Particle size	mm	-	1.68-2.00	1.68-2.00	1.68-2.00	1.68-2.00	1.68-2.00

LB = Linear bond
PB= Parallel Bond

			K Ratio(LB)				
Symbol	Units	Material Properties	KLB_0.35	KLB_1.35	Initial	KLB_3.35	KLB_4.35
Gap	m	Gap length	2.00E-04	2.00E-04	2.00E-04	2.00E-04	2.00E-04
σ_c	Pascal	Tension strength	3.00E+05	3.00E+05	3.00E+05	3.00E+05	3.00E+05
c	Pascal	Cohesion	3.00E+05	3.00E+05	3.00E+05	3.00E+05	3.00E+05
Φ	Degrees^o	Friction angle	70.00	70.00	70.00	70.00	70.00
μ	-	Particle friction	0.70	0.70	0.70	0.70	0.70
E(LB)	Pascal	Young's Modulus	7.90E+09	7.90E+09	7.90E+09	7.90E+09	7.90E+09
E*(PB)	Pascal	Young's Modulus	7.90E+09	7.90E+09	7.90E+09	7.90E+09	7.90E+09
K(LB)	-	Krat (kn/ks)	0.35	1.35	2.35	3.35	4.35
K*(PB)	-	Krat (kn/ks)	2.35	2.35	2.35	2.35	2.35
Particle size	mm	-	1.68-2.00	1.68-2.00	1.68-2.00	1.68-2.00	1.68-2.00

LB = Linear bond
PB= Parallel Bond

			μ				
Symbol	Units	Material Properties	MU_0.30	MU_0.50	Initial	MU_0.90	MU_1.10
Gap	m	Gap length	2.00E-04	2.00E-04	2.00E-04	2.00E-04	2.00E-04
σ_c	Pascal	Tension strength	3.00E+05	3.00E+05	3.00E+05	3.00E+05	3.00E+05
c	Pascal	Cohesion	3.00E+05	3.00E+05	3.00E+05	3.00E+05	3.00E+05
Φ	Degrees^o	Friction angle	70.00	70.00	70.00	70.00	70.00
μ	-	Particle friction	0.30	0.50	0.70	0.90	1.10
E(LB)	Pascal	Young's Modulus	7.90E+09	7.90E+09	7.90E+09	7.90E+09	7.90E+09
E*(PB)	Pascal	Young's Modulus	7.90E+09	7.90E+09	7.90E+09	7.90E+09	7.90E+09
K(LB)	-	Krat (kn/ks)	2.35	2.35	2.35	2.35	2.35
K*(PB)	-	Krat (kn/ks)	2.35	2.35	2.35	2.35	2.35
Particle size	mm	-	1.68-2.00	1.68-2.00	1.68-2.00	1.68-2.00	1.68-2.00

LB = Linear bond
PB= Parallel Bond

			Particle size				
Symbol	Units	Material Properties	PS_1.04	PS_1.36	Initial	PS_2.00	PS_2.32
Gap	m	Gap length	2.00E-04	2.00E-04	2.00E-04	2.00E-04	2.00E-04
σ_c	Pascal	Tension strength	3.00E+05	3.00E+05	3.00E+05	3.00E+05	3.00E+05
c	Pascal	Cohesion	3.00E+05	3.00E+05	3.00E+05	3.00E+05	3.00E+05
Φ	Degrees^o	Friction angle	70.00	70.00	70.00	70.00	70.00
μ	-	Particle friction	0.70	0.70	0.70	0.70	0.70
E(LB)	Pascal	Young's Modulus	7.90E+09	7.90E+09	7.90E+09	7.90E+09	7.90E+09
E*(PB)	Pascal	Young's Modulus	7.90E+09	7.90E+09	7.90E+09	7.90E+09	7.90E+09
K(LB)	-	Krat (kn/ks)	2.35	2.35	2.35	2.35	2.35
K*(PB)	-	Krat (kn/ks)	2.35	2.35	2.35	2.35	2.35
Particle size	mm	-	1.04-1.36	1.36-1.68	1.68-2.00	2.00-2.32	2.32-2.64

LB = Linear bond
PB= Parallel Bond

The concrete block parametric combination tables are presented.

			Tensile Strength (concrete block)				
Symbol	Units	Material Properties	T_6.00	T_8.00	Initial	T_12.00	T_14.00
Gap	m	Gap length	6.00E-04	6.00E-04	6.00E-04	6.00E-04	6.00E-04
σ_c	Pascal	Tension strength	6.00E+06	8.00E+06	1.00E+07	1.20E+07	1.40E+07
c	Pascal	Cohesion	4.00E+06	4.00E+06	4.00E+06	4.00E+06	4.00E+06
Φ	Degrees^o	Friction angle	70.00	70.00	70.00	70.00	70.00
μ	-	Particle friction	0.60	0.60	0.60	0.60	0.60
E(LB)	Pascal	Young's Modulus	3.25E+09	3.25E+09	3.25E+09	3.25E+09	3.25E+09
E*(PB)	Pascal	Young's Modulus	3.25E+09	3.25E+09	3.25E+09	3.25E+09	3.25E+09
K(LB)	-	Krat (kn/ks)	5.00	5.00	5.00	5.00	5.00
K*(PB)	-	Krat (kn/ks)	5.00	5.00	5.00	5.00	5.00
Particle size	mm	-	4.00-6.00	4.00-6.00	4.00-6.00	4.00-6.00	4.00-6.00

LB = Linear bond
PB= Parallel Bond

			Cohesion (concrete block)				
Symbol	Units	Material Properties	C_0.50	C_2.50	Initial	C_5.50	C_7.00
Gap	m	Gap length	6.00E-04	6.00E-04	6.00E-04	6.00E-04	6.00E-04
σ_c	Pascal	Tension strength	1.00E+07	1.00E+07	1.00E+07	1.00E+07	1.00E+07
c	Pascal	Cohesion	5.00E+05	2.50E+06	4.00E+06	5.50E+06	7.00E+06
Φ	Degrees^o	Friction angle	70.00	70.00	70.00	70.00	70.00
μ	-	Particle friction	0.60	0.60	0.60	0.60	0.60
E(LB)	Pascal	Young's Modulus	3.25E+09	3.25E+09	3.25E+09	3.25E+09	3.25E+09
E*(PB)	Pascal	Young's Modulus	3.25E+09	3.25E+09	3.25E+09	3.25E+09	3.25E+09
K(LB)	-	Krat (kn/ks)	5.00	5.00	5.00	5.00	5.00
K*(PB)	-	Krat (kn/ks)	5.00	5.00	5.00	5.00	5.00
Particle size	mm	-	4.00-6.00	4.00-6.00	4.00-6.00	4.00-6.00	4.00-6.00
LB = Linear bond PB= Parallel Bond							

			E(PB) (concrete block)				
Symbol	Units	Material Properties	EPB_1.25	EPB_2.25	Initial	EPB_4.25	EPB_5.25
Gap	m	Gap length	6.00E-04	6.00E-04	6.00E-04	6.00E-04	6.00E-04
σ_c	Pascal	Tension strength	1.00E+07	1.00E+07	1.00E+07	1.00E+07	1.00E+07
c	Pascal	Cohesion	4.00E+06	4.00E+06	4.00E+06	4.00E+06	4.00E+06
Φ	Degrees^o	Friction angle	70.00	70.00	70.00	70.00	70.00
μ	-	Particle friction	0.60	0.60	0.60	0.60	0.60
E(LB)	Pascal	Young's Modulus	3.25E+09	3.25E+09	3.25E+09	3.25E+09	3.25E+09
E*(PB)	Pascal	Young's Modulus	1.25E+09	2.25E+09	3.25E+09	4.25E+09	5.25E+09
K(LB)	-	Krat (kn/ks)	5.00	5.00	5.00	5.00	5.00
K*(PB)	-	Krat (kn/ks)	5.00	5.00	5.00	5.00	5.00
Particle size	mm	-	4.00-6.00	4.00-6.00	4.00-6.00	4.00-6.00	4.00-6.00

LB = Linear bond
PB= Parallel Bond

			E(LB) (concrete block)				
Symbol	Units	Material Properties	ELB_1.25	ELB_2.25	Initial	ELB_4.25	ELB_5.25
Gap	m	Gap length	6.00E-04	6.00E-04	6.00E-04	6.00E-04	6.00E-04
σc	Pascal	Tension strength	1.00E+07	1.00E+07	1.00E+07	1.00E+07	1.00E+07
c	Pascal	Cohesion	4.00E+06	4.00E+06	4.00E+06	4.00E+06	4.00E+06
Φ	Degrees^{o}	Friction angle	70.00	70.00	70.00	70.00	70.00
μ	-	Particle friction	0.60	0.60	0.60	0.60	0.60
E(LB)	Pascal	Young's Modulus	1.25E+09	2.25E+09	3.25E+09	4.25E+09	5.25E+09
E*(PB)	Pascal	Young's Modulus	3.25E+09	3.25E+09	3.25E+09	3.25E+09	3.25E+09
K(LB)	-	Krat (kn/ks)	5.00	5.00	5.00	5.00	5.00
K*(PB)	-	Krat (kn/ks)	5.00	5.00	5.00	5.00	5.00
Particle size	mm	-	4.00-6.00	4.00-6.00	4.00-6.00	4.00-6.00	4.00-6.00

LB = Linear bond
PB= Parallel Bond

			Friction angle (concrete block)				
Symbol	Units	Material Properties	FA_50	FA_60	Initial	FA_80	FA_90
Gap	m	Gap length	6.00E-04	6.00E-04	6.00E-04	6.00E-04	6.00E-04
σ_c	Pascal	Tension strength	1.00E+07	1.00E+07	1.00E+07	1.00E+07	1.00E+07
c	Pascal	Cohesion	4.00E+06	4.00E+06	4.00E+06	4.00E+06	4.00E+06
Φ	Degrees^o	Friction angle	50.00	60.00	70.00	80.00	89.00
μ	-	Particle friction	0.70	0.70	0.70	0.70	0.70
E(LB)	Pascal	Young's Modulus	3.25E+09	3.25E+09	3.25E+09	3.25E+09	3.25E+09
E*(PB)	Pascal	Young's Modulus	3.25E+09	3.25E+09	3.25E+09	3.25E+09	3.25E+09
K(LB)	-	Krat (kn/ks)	5.00	5.00	5.00	5.00	5.00
K*(PB)	-	Krat (kn/ks)	5.00	5.00	5.00	5.00	5.00
Particle size	mm	-	4.00-6.00	4.00-6.00	4.00-6.00	4.00-6.00	4.00-6.00

LB = Linear bond
PB= Parallel Bond

			K Ratio(PB) (concrete block)				
Symbol	Units	Material Properties	KPB_1.00	KPB_3.00	Initial	KPB_7.00	KPB_9.00
Gap	m	Gap length	6.00E-04	6.00E-04	6.00E-04	6.00E-04	6.00E-04
σ_c	Pascal	Tension strength	1.00E+07	1.00E+07	1.00E+07	1.00E+07	1.00E+07
c	Pascal	Cohesion	4.00E+06	4.00E+06	4.00E+06	4.00E+06	4.00E+06
Φ	Degrees^o	Friction angle	70.00	70.00	70.00	70.00	70.00
μ	-	Particle friction	0.70	0.70	0.70	0.70	0.70
E(LB)	Pascal	Young's Modulus	3.25E+09	3.25E+09	3.25E+09	3.25E+09	3.25E+09
E*(PB)	Pascal	Young's Modulus	3.25E+09	3.25E+09	3.25E+09	3.25E+09	3.25E+09
K(LB)	-	Krat (kn/ks)	5.00	5.00	5.00	5.00	5.00
K*(PB)	-	Krat (kn/ks)	1.00	3.00	5.00	7.00	9.00
Particle size	mm	-	4.00-6.00	4.00-6.00	4.00-6.00	4.00-6.00	4.00-6.00
LB = Linear bond PB= Parallel Bond							

			K Ratio(LB) (concrete block)				
Symbol	Units	Material Properties	KLB_1.00	KLB_3.00	Initial	KLB_7.00	KLB_9.00
Gap	m	Gap length	6.00E-04	6.00E-04	6.00E-04	6.00E-04	6.00E-04
σ_c	Pascal	Tension strength	1.00E+07	1.00E+07	1.00E+07	1.00E+07	1.00E+07
c	Pascal	Cohesion	4.00E+06	4.00E+06	4.00E+06	4.00E+06	4.00E+06
Φ	Degrees^o	Friction angle	70.00	70.00	70.00	70.00	70.00
μ	-	Particle friction	0.70	0.70	0.70	0.70	0.70
E(LB)	Pascal	Young's Modulus	3.25E+09	3.25E+09	3.25E+09	3.25E+09	3.25E+09
E*(PB)	Pascal	Young's Modulus	3.25E+09	3.25E+09	3.25E+09	3.25E+09	3.25E+09
K(LB)	-	Krat (kn/ks)	1.00	3.00	5.00	7.00	9.00
K*(PB)	-	Krat (kn/ks)	5.00	5.00	5.00	5.00	5.00
Particle size	mm	-	4.00-6.00	4.00-6.00	4.00-6.00	4.00-6.00	4.00-6.00

LB = Linear bond
PB= Parallel Bond

			μ(concrete block)				
Symbol	Units	Material Properties	MU_0.20	MU_0.40	Initial	MU_0.80	MU_1.00
Gap	m	Gap length	6.00E-04	6.00E-04	6.00E-04	6.00E-04	6.00E-04
σ_c	Pascal	Tension strength	1.00E+07	1.00E+07	1.00E+07	1.00E+07	1.00E+07
c	Pascal	Cohesion	4.00E+06	4.00E+06	4.00E+06	4.00E+06	4.00E+06
Φ	Degrees^o	Friction angle	70.00	70.00	70.00	70.00	70.00
μ	-	Particle friction	0.20	0.40	0.60	0.80	1.00
E(LB)	Pascal	Young's Modulus	3.25E+09	3.25E+09	3.25E+09	3.25E+09	3.25E+09
E*(PB)	Pascal	Young's Modulus	3.25E+09	3.25E+09	3.25E+09	3.25E+09	3.25E+09
K(LB)	-	Krat (kn/ks)	5.00	5.00	5.00	5.00	5.00
K*(PB)	-	Krat (kn/ks)	5.00	5.00	5.00	5.00	5.00
Particle size	mm	-	4.00-6.00	4.00-6.00	4.00-6.00	4.00-6.00	4.00-6.00

LB = Linear bond
PB= Parallel Bond